研究課題名：パラメトリックＸ線 LEBRA-PXR を用いた生体硬組織結晶の微小部解析と自由電子レーザーLEBRA-FEL を用いた歯科レーザー治療のＥＢＭに対する基礎的研究と最適条件の決定*

研究代表者：寒河江　登志朗(日本大学松戸歯学部)
共同研究者：岡田　裕之（日本大学松戸歯学部）
佐藤由紀江（日本大学松戸歯学部）
中田　浩史（日本大学松戸歯学部）
R.Z. LeGeros (New York Univ. College of Dentistry)
中井　泉　（東京理科大理学部）
筧　光夫　（明海大学歯学部）
松村恵美子（日本大学松戸歯学研究科大学院）
佐藤　俊紀（日本大学松戸歯学研究科大学院）
豊田　千枝（日本大学松戸歯学研究科大学院）
諏訪　武利（日本大学松戸歯学研究科大学院）

【研究概要】

電子線利用研究施設，LEBRA，のパラメトリック X 線，PXR，と自由電子レーザー，FEL，を利用した本実験と，予備実験装置（IP 型微小部 X 線回折装置，PSPC 型微小部 X 線回折装置，粉末 X 線回折装置）を利用した研究の成果.

1) LEBRA-PXR

LEBRA 施設の作り出す PXR は実用研究にむけた PXR としては世界的に初めてのものといわれている．この PXR を実際の実験に用いるための予察的実験を，透過像撮影と回折実験を通して行い，あわせて LEBRA-PXR の諸特性を明らかにし，応用実験への基礎的データとしていった.

1-1) LEBRA-PXR による X 線透過像観察，Radiography

X 線の物質透過性はいわゆるレントゲン撮影など多方面に利用されている．X 線の透過能は物質の組成・密度などによって異なる．ここでは LEBRA-PXR の波長可変性を利用して，実験的にフッ素による障害を起こさせたラットの骨の比較を行った（in preparation）.

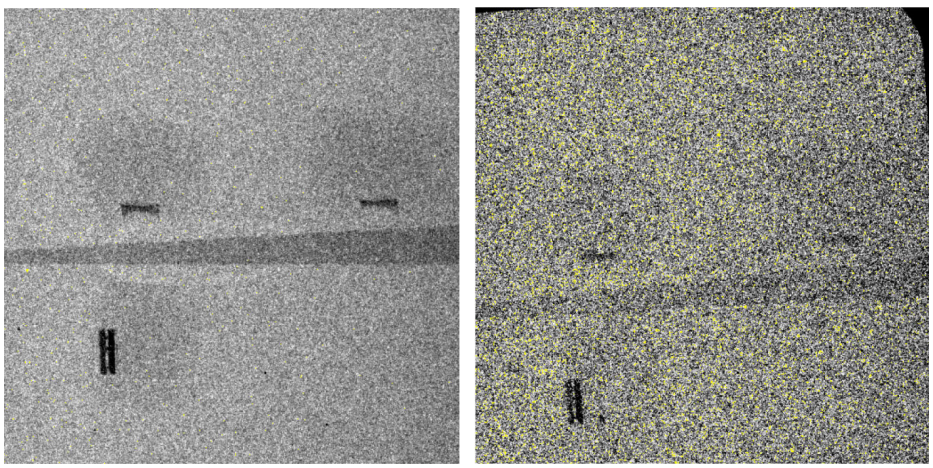

Fig. 1.1. Radiograms of the F-treated rat bone sections (upper) and non-treated rat bone sections (lower). Left: X-ray energy: 7.0 KeV (1.77 Å). Right: X-ray energy; 10.0 KeV (1.24 Å). The left radiogram showed the clearer images of rat bone sections than the right one.

LEBRA-PXR を用いた X 線透過像観察は、共同研究者の中田浩史ら、諏訪武利ら、佐藤俊成らによっても行われている（2005 年 LEBRA 総合研究発表会)。

1-2) LEBRA-PXR による X 線吸収端構造解析，XAFS

元素は X 線の波長に依存した特有の X 線吸収曲線を描く．特定の波長の前後で X 線吸収能は極端に変化する (X 線吸収端)．この性質を利用すると元素の特定が出来ることが知られており、XAFS（X-ray Absorption Fine Structure）分析法として活用されている．さらに X 線吸収端近傍スペクトル XANES（X-ray Absorption Near Edge Spectra）と X 線吸収端微細構造 EXAFS（Extended X-ray Absorption Fine Structure）解析法が確立されており、この方法によると元素自身の状態と元素の周囲の環境解析が可能である。

ここでは恐竜の卵化石中に認められた白色を呈する不明物質のついて LEBRA-PXR の波長を変えて探索した結果，Sr が含有されていることが明らかとなった（今回発表)．

Fig. 1.2.1. Photographs of the fossil Titanosaurus egg shell section.

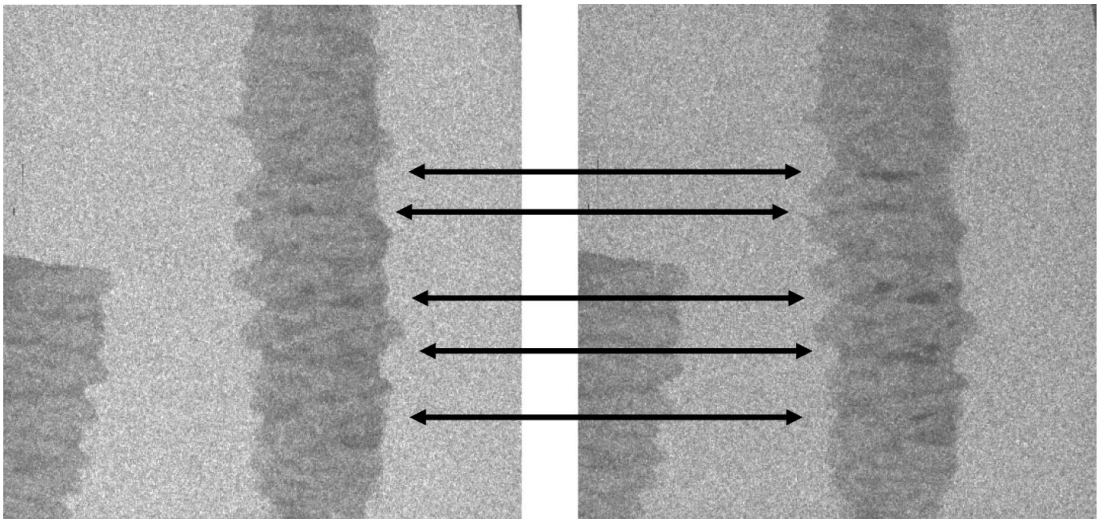

Fig. 1.2.2. LEBRA-PXR radiograms of the Titanosaurus egg shell sections.
Left: X-ray energy; 16.0 KeV (0.775 Å). Right: X-ray energy 16.2 KeV (0.765 Å).
X-ray absorption K edge for Sr is 16.10 KeV (0.7699 Å). The higher the X-ray energy, the greater the X-ray absorption of the interested material. Note the left and right ends of the arrows.

1-3) LEBRA-PXR による X 線回折実験，Diffraction

LEBRA-PXR を利用した X 線回折実験用に IP 型微小部 X 線回折記録装置が準備されている．こ

れは LEBRA-PXR を集光系を通して試料の 1 点に X 線を照射する構成となっている. 現在の段階ではまだ集光系の調整が完全ではないため，この IP 型微小部 XRD は使用していない.

その前段階として，普及型の X 線回折計を利用して，LEBRA-PXR を直接に試料に照射して，回折 X 線が記録できるか試したところ，回折実験は成功し，さらに LEBRA-PXR が結晶性の評価に優れた能力を有していることが明らかとなった(投稿中).

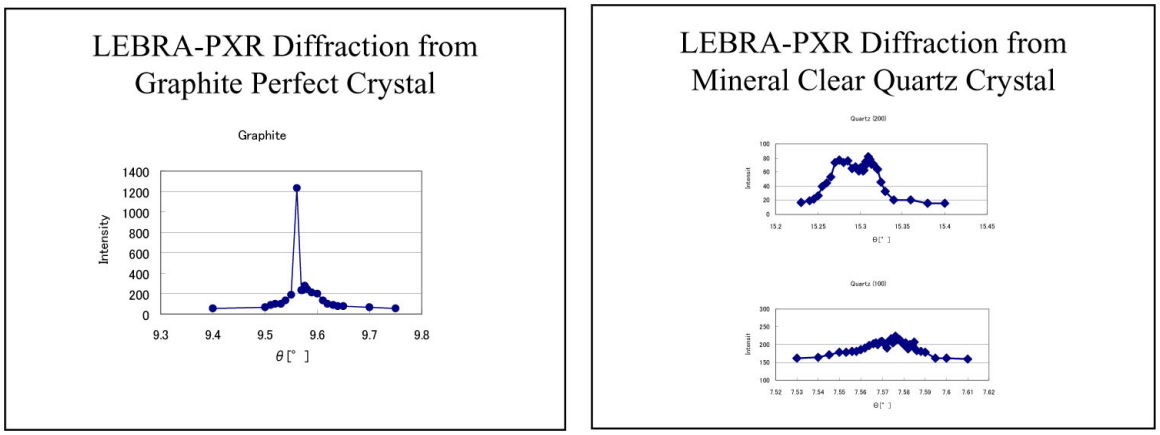

Fig. 1.3.1 LEBRA-PXR XRD pattern for the Graphite and mineral Quartz crystals.

2) LEBRA-FEL

歯科におけるレーザーの利用は、歯のう蝕部位の削除、歯石の除去、歯質の強化、歯肉切除、病理的な変性部位の切除など広範囲に及んでいる。FEL はパルス構造など様々な点において臨床応用されているレーザー機器と異なった特性を有している.

ここでは歯のエナメル質と象牙質にレーザー照射した場合に、臨床で使われているレーザーと LEBRA-FEL ではその違いがどこに現れてくるか予察的な実験を行い，特に結晶レベルで変化を LEBRA 施設の予備実験用 X 線回折装置で比較した.

2-1) 同一波長における LEBRA-FEL と従来型レーザー装置との比較

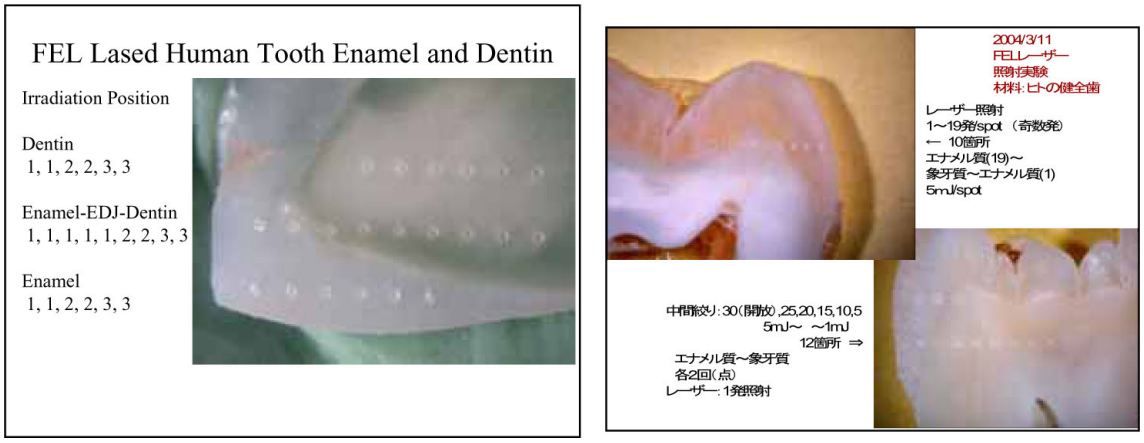

Fig. 2.1. Irradiation of 2.94 μm LEBRA-FEL on the human tooth enamel and dentin. Numbers in the figure were the numbers of LEBRA-FEL shot. The depth of pit was in relation to the number of shot. No apparent scorch was observed on the pits both at the enamel and dentin.

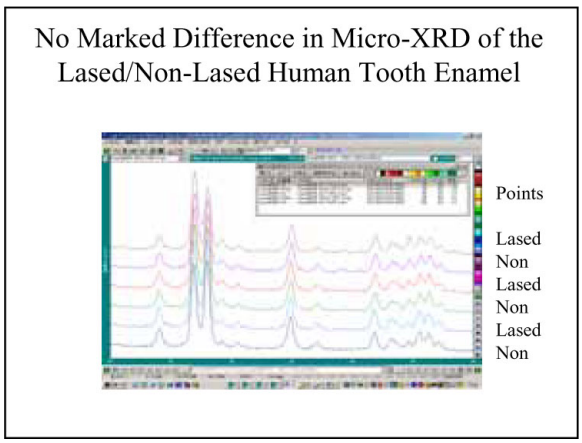

Fig. 2.2. Micro-XRD patterns of the irradiated and non-irradiated enamel showed that there was no crystallographic change.

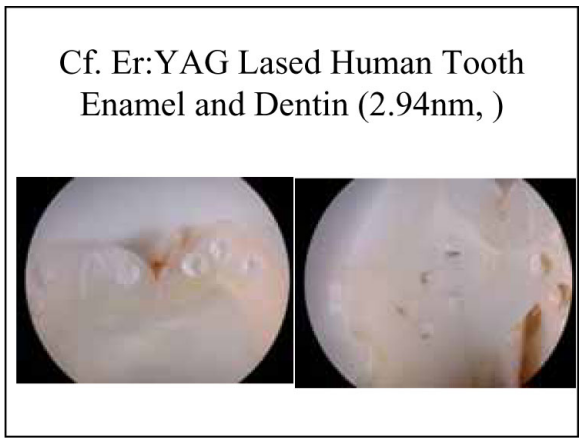

Fig. 2.3. Reference study using a 2.94 μm Er:YAG laser showed that there were apparent scorches in the irradiation pits of dentin.

2-2) LEBRA-FEL の波長可変性を利用した研究

LEBRA-FEL の波長可変の特徴を利用して，波長を 2.6 μm から 4.0 μm までの範囲で歯に照射実験を行った．その結果，3.0 μm を中心とした波長で歯に対する pit 形成が顕著であるが，その波長から外れるにしたがって pit 形成は衰弱した．これにより，従来歯に対するレーザー照射効果は 3.0 μm が最適であるという予測が実験的に裏付けられた．

しかし，細かく波長を刻んだ実験では，歯のエナメル質と象牙質において pit 形成に最適な波長に若干の違いが認められた（未発表）．このことは，レーザー照射の効果は対象物の組成と構造の違いに関連することを改めて示したものと考える．さらに詳細な実験研究が必要である．

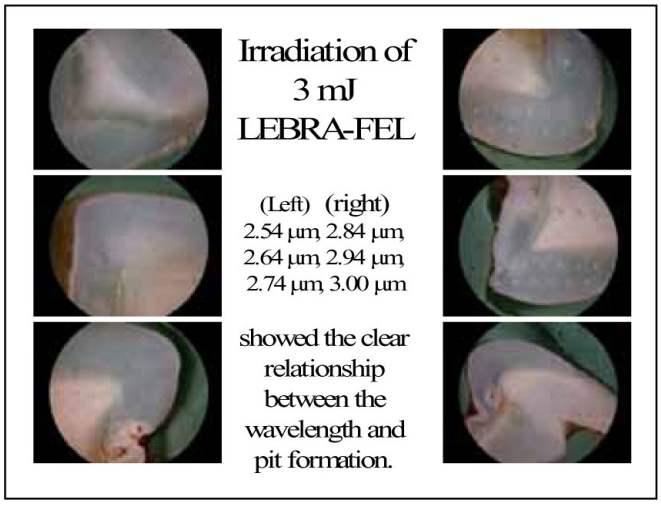

Fig.2.4

3) LEBRA-PowderXRD

粉末 X 線回折計は物質同定の基本的な分析装置である．LEBRA では 18 kW ローター型強力 X 線発生装置と組み合わせた RINT-2000（Rigaku）を導入して，測定時間の短縮と精度向上を図っている．この装置は LEBRA-PXR を用いた X 線回折実験の予備実験装置としての位置づけが成されており、試料選定あるいは粉末状試料の解析に使っている。

結晶構造解析は単結晶を用いて行われるのが一般的であるが、試料量・状態など制約が多い場合

には粉末試料で Reitveld 法などの結晶構造解析を行うことが可能である。生体内に出現する結晶性物質は大概において単結晶を得ることは困難であり、粉末試料による結晶解析が選択されざるを得ない。たとえば、歯のエナメル質を構成する生体アパタイトは、生体内に出現するアパタイトとしては結晶性も結晶粒子の大きさも最高最大であるが、その大きさは長さで最大 1000Å程度であり幅は 100Å以下であると考えられている。また、結晶の組成は PO_4^{3-}を CO_3^{2-}が置換していると言う生体アパタイトの特徴を有するため、再結晶化などで単結晶化するともともとの結晶とは異なったものとなってしまう。

このような粉末状試料である歯のエナメル質の結晶解析に粉末法 X 線回折による研究を行っている。生体の造りだす物質の常として、個体間および個体内変異が大きいことが知られている。エナメル質も例外ではなく、その変異の幅の解析と原因の追究を行っている。

4) LEBRA PSPC-microXRD

ローター型強力 X 線発生装置と組み合わせた位置検出型の湾曲 PSPC（position sensitive proportional counter）は㈱リガクの独自製品であり，微小焦点コリメータと組み合わせて 100 μm から 10 μm の微小領域の XRD 情報を短時間に得ることが出来る.

この装置を利用して調べたところ，恐竜 Titanosaurus の化石卵がもともとの結晶である炭酸カルシウムから一部分は変質してケイ酸塩，quartz，から構成されていることが明らかとなった（投稿中）.

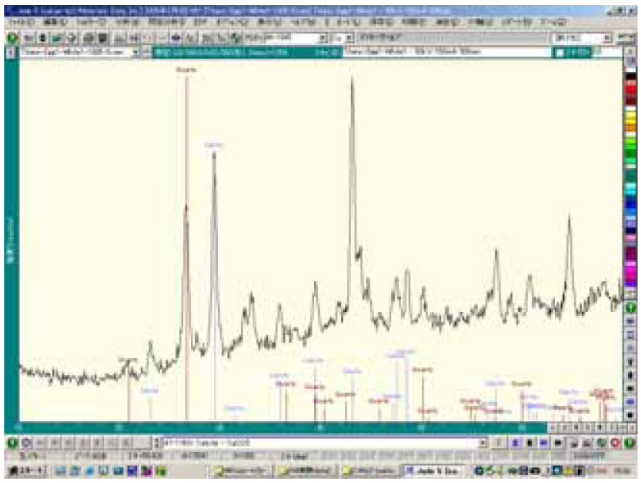

Fig. 4.1. PSPC micro-XRD pattern for the Titanosaurs egg shell.

この装置を用いて共同研究者の豊田千枝・岡田裕之らによる唾石の組成・構造分析および形成過程の研究、中田浩史・諏訪武利・早川徹らによる Ti-Implant の骨形成能の研究、佐藤俊成らの骨芽細胞培養系における形成された石灰化物の分析、筧・LeGeros らによる骨形成におけるフッ素の影響の研究などが行われている（2005 年 LEBRA 総合研究発表会）。

5) LEBRA IP-microXRD

IP 型微小部 XRD 装置は試料からの回折 X 線を 2 次元の Imaging Plate で受け止めることで，結晶配列などの結晶組織を解析できる.

ここでは歯のエナメル質を構成するアパタイト結晶の配向について研究した例を示す.

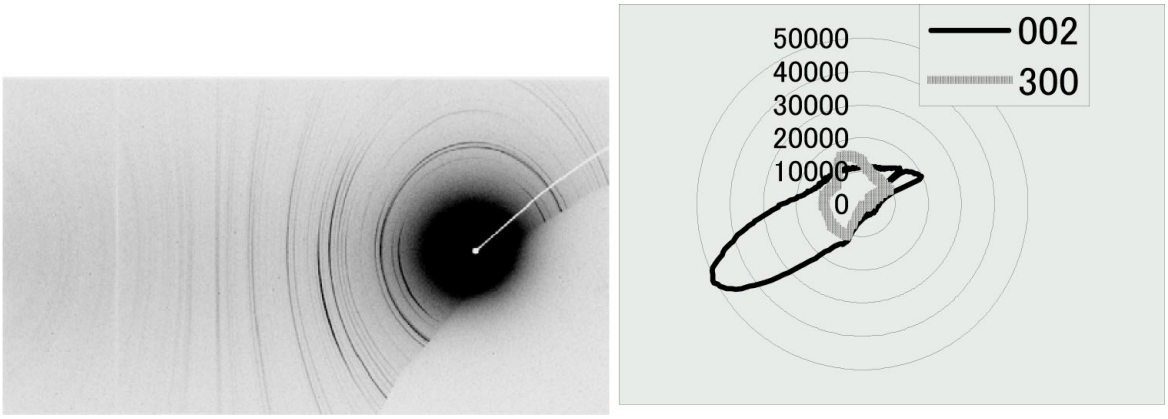

Fig 5.1. A) XRD-IP image of the enamel sample #1.

The numbers in the figure were the reflection indexes of apatite. Note all the reflections were in the arc form. The lower-right half was the portion of the shadow by the sample holder stage. The shadow of the beam stopper was seen at the right-upper direction. These shadows were common in this study. B) Radar chart for the intensity distribution of the 002 reflection, bold line, and the 300 reflection, dashed line, in Fig. 1A. The numbers were the intensity.

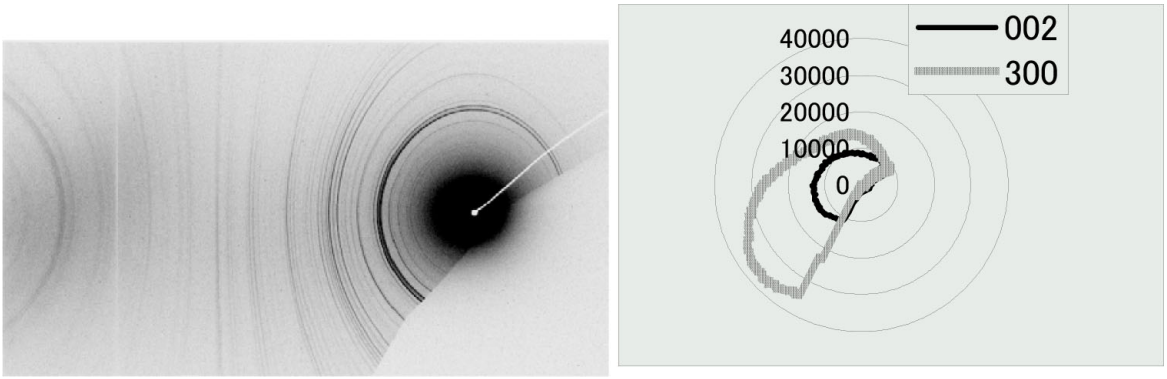

Fig. 5.1. C) XRD-IP image of the enamel sample #1.

The sample was rotated 90 degrees around the sample rotation axis ϕ from the position in Fig. 1A. D) Radar chart for the intensity distribution of the 002 reflection, bold line, and 300 reflection, dashed line, in Fig. 1C. Note the intensity of the 300 reflection was not even at the opposite side.

【研究業績等】

・発表論文

(1) Toshiro Sakae, Hirokazu Oinuma, Masanori Higa and Yukishige Kozawa; "X-ray Diffraction and FTIR Study on Heating Effects of Dentin from Mammoth Tusk", J. Oral Biosci. 47(1): 83-88,2005

(2) Emiko Matsumura; "A Morphological Study of Biomimetic Approach for Pathological Calcification In Vitro", Int. J. Oral-Med. Sci., 2(1): 23-32, 2004

(3) T.HAYAKAWA, M.YOSHINARI, T.SAKAE and K.NEMOTO; "Calcium phosphate formation on the phosphorylated dental bonding agent in electrolyte solution", Journal of Oral Rehabilitation, 2004, 31; 67-73

(4) Yoshiaki Akimoto, Toshiro Sakae, Chie Toyoda, Makiko Ono, Kazuhiro Hasegawa, Shigeo TANAKA, Jun Shibutani, Takashi Kaneda, Takeshi Maeda, Teruyasu Hirayama, Akira Fujii, Hirotsugu Yamamoto and Racquel.Z.LeGeros; "An Unusually Large Submandibular Salivary Calculus: Case Report and Structural Analysis", Int. J. Oral-Med. Sci., 2(1): 50-53,2004

(5) Toshiro SAKAE, Yoshiaki AKIMOTO, Takashi KANEDA, Akira FUJII, Tadahiko UTSUNOMIYA, Hirotsugu YAMAMOTO, Takaatsu HARADA, Kazuo HIGUCHI, Seiichi SATO and Racquel.Z.LeGeros; "Intermittent Crystal Growth of Unusually Long Submandibular Sialolith Revealed by Micro-Focus- and Selected-Area- X-Ray Diffraction", Journal of Hard Tissue Biology, 12[1](2003) p25-28

(6) T.Sakae, A.Ookubo, R.Z.LeGeros, R.Shimogoryou, Y.Sato, S.Lin, H.Yamamoto, Y.Kozawa; "Bone Formation Induced by Several Carbonate- and Fluoride- Containing Apatite implanted in Dog Mandible", Key Engineering Materials, Vols.240-242 (2003) pp.395-398

(7) T. Hayakawa, K. Nemoto, T. Sakae, M. Yoshinari; "Calcium phosphate deposition on dentin bonding agent in electrolyte solution", Proceedings of the International Conference on Dentin/Pulp Complex 2001, 15, 2001, 140-142

(8) 野崎泰夫、寒河江登志朗; "ヒトのエナメル質比重分画によるアパタイト結晶中の炭酸イオン分配比率と含有水比率の推定", 日大口腔科学, 27, 2001, 73-79

(9) 松村恵美子、宇都宮忠彦、寒河江登志朗、R.Z. LeGeros、山本浩嗣; "動脈硬化症にみられた興味ある結晶構造物に関する一知見", 日大口腔科学, 27, 2001, 80-84

(10) Y. Asada, Y. Sato, T. Shimizu, T. Sakae, H. Yamamoto, T. Maeda; "Genptyping of heterogeneous osteopetroic mice using microsatellite makers", Jpn. J. oral Biol, 44, 2002, 1-6

・学会発表

(1) Sakae, T., Sato, Y., Okada, H., Yamamoto, H., Hayakawa, T., Nakada, H., Hayakawa, Y., Tanaka, T., Hayakawa, K., Sato, I.; "Application of LEBRA-PXR to Dental Hard Tissues, JADR", Japanese Association for Dental Research, A Japanese Division of International Association for Deantal Research,Tokyo,2004/11/27

(2) 寒河江登志朗，佐藤由紀江，山本浩嗣早川恭史，田中俊成，早川　建，佐藤　勇; "歯のエナメル質と象牙質に対する自由電子レーザー（FEL)照射とEr：YAGレーザー照射の比較", 日本レーザー医学会，東京, 2004/11/11

(3) H. Nakada, T. Sakae, R.Z. LeGeros, T. Kato, T. Machida, K. Kobayashi; "Characteristics of newly

generated bone around dental Ti implant", 8th Int Conf on Chemistry and Biology of Mineralized Tissue, Banff, Canada, 2004/10/17-22

(4) 寒河江登志朗，佐藤由紀江，山本浩嗣 ，佐藤　勇; "2.94μm自由電子レーザーのエナメル質へのablation効果", 歯科基礎医学会, 広島, 2004/9/25

(5) 寒河江登志朗，佐藤　勇，早川　建，田中俊成，早川恭史; "LEBRA-PXRによる生体材料のラジオグラフィとXAFS実験", 日本鉱物学会, 岡山, 2004/9/22

(6) T. SAKAE,　K. SUZUKI, Y. KOZAWA, H. MISHIMA; "Three-Dimensional Analysis of Prism Decussation in Tooth Enamel from Human and Several Animals Using A Micro Focus X-ray Diffraction.", 16th IFAA, Int Federation of Anatomy Association, Kyoto, 2004/8/25

(7) T. Sakae; "10um Scale Analysis of Enamel Crystals by X-ray Micro-Diffraction", JADR, Japanese Association for Dental Research, A Japanese Division of International Association for Deantal Research, Oosaka, 2003/12/1

(8) 寒河江登志朗; "歯のエナメル質結晶の配向特性の再検討", 日本鉱物学会, 仙台, 2003/10/1

(9) 寒河江登志朗，鈴木秀敏，鈴木久仁博，岩佐由香，小澤幸重; "白濁を呈するエナメル質の微小部X線回折と顕微FT-IRによる２次元結晶解析", 歯科基礎医学会, 盛岡, 2003/9/18

(10) 寒河江登志朗*、鈴木久仁博*、小澤幸重*（日本大学・松戸歯学部・第2解剖*）; "ウシエナメル質ハンター・シュレーゲル条の結晶方位について", 日本解剖学会関東地方会, 鶴見大学, 2003

J. Oral Biosci. 47(1) : 83-88, 2005

ORIGINAL

X-ray Diffraction and FTIR Study on Heating Effects of Dentin from Mammoth Tusk

Toshiro Sakae[§], Hirokazu Oinuma, Masanori Higa and Yukishige Kozawa

Department of Anatomy II, Nihon University School of Dentistry at Matsudo
(Chief : Prof. Yukishige Kozawa)
2-870-1 Sakaecho-nishi, Matsudo, Chiba 271-8587, Japan
〔Received on August 24 ; Accepted on November, 6〕

Key words : mammoth/dentin/thermal/XRD/FTIR

Abstract : Heating effects on dentin from mammoth tusks were examined by means of X-ray diffraction (XRD) and Fourier transform infrared spectrometric (FTIR), techniques. Dentin samples were sectioned into rectangular plates of about 10×5×1mm in size, using a low speed diamond saw. Heating treatment was carried out using a differential thermal analyzer. It was shown that the organic materials of the dentin were about 32 wt%, and combusted at a temperature range of 200℃ to 600℃, showing the coupled exotherm resulting in the release of the inorganic apatite phase from the closely related dentin collagen, and that the exotherm at 700℃ related to the crystalline phase transformation from the intermediate phase to crystalline β-TCP. This study suggested that the magnesium components in mammoth tusk dentin manage or control the crystalline phase transformation.

Introduction

Dentin has been widely used as a native biological material in a variety of research fields, such as caries mechanism[1] and adhesive experiments[2]. Recently laser applications in dental clinic have grown radically. The study of mechanical and/or thermal ablation mechanisms of lasers to dentin is needed, and we need to know the heating effects or thermal changes of dentin in more detail[3]. However, only a limited number of studies have been carried out on the thermal properties of dentin[4-13]. Besides the structure of dentin, human dentin has a varied chemical composition[14]. Therefore, standard dentin material for experimental use is required immediately.

Dentin from mammoth tusk may be a good candidate for experimental use because of its volume and uniformity. It is widely used for cell culture, though little is known about elephant tusk dentin structure and chemical composition[15-17]. This study aimed to clarify the effects of heating on mammoth dentin, to provide basic knowledge of the thermal behavior of dentin.

Materials and Methods

The mammoth tusk used in this study (about 10 cm in diameter) was obtained through an importer. Based on the pattern of the sectioned plane of tusk, the material was identified as that of fossil *Mammuthus* sp. The surface was colored brown, but the inside was white and had a lustre similar to ivory. Plates, about 10×5×1mm, were sectioned from the outer part of the dentin using a Buhler low speed diamond saw.

§ Corresponding author
E-mail : sakae@mascat.nihon-u.ac.jp

Table 1 Results of TG, XRD, FTIR and colors after the heating treatments *

		TG	XRD			FTIR	
Sample	Color	Wt loss % in TG	HA	Intm	TCP	Organic	Inorganic
r.t.	Natural	–	Low XL	–	–	+ +	Ap
100 ℃	Natural		Low XL	–	–	+ +	Ap
200 ℃	Natural	16	Low XL	–	–	Start decay	Ap
300 ℃	Natural		Low XL	–	–	Decaying	Ap
400 ℃	Natural	21	Low XL	–	–	Weaken & broaden	Ap
500 ℃	Sooty gray			Low XL	–		Intm
600 ℃	Brownish	11	–	Low XL	–		Intm
700 ℃	Brownish		–	–	Low XL		TCP
800 ℃	White	1	–	–	XL		TCP
900 ℃	White		–	–	XL		TCP
1,000 ℃	White	< 0.2	–	–	XL		TCP
1,100 ℃	White		–	–	XL		TCP
1,200 ℃	White	< 0.1	–	–	XL		TCP

* : Low XL : low crystalline, XL : well crystalline, Ap : apatite, Intm : intermediate, TCP : β-tricalcium phosphate.

Heating treatment was carried out using a RIGAKU laser-furnace thermogravimetric-differential thermal analyzer, TG-DTA. The samples were heated to the set-up temperatures, 100℃ interval between 100℃ and 1,100℃, with an ascending rate of 5℃/min in a static atmosphere. The heating was quickly stopped when the sample reached the set-up temperature and rapidly cooled to room temperature using an air blow system.

X-ray diffraction (XRD) data was obtained by a RIGAKU-PSPC, position-sensitive-proportional-counter micro-XRD system under the following conditions : X-ray generator : rotary type Cu target, accelerating voltage : 50kV, current : 300 mA, X-ray beam collimeter : 30 μm, sample position : 10 degree to the incident beam, sample movement : rotation at 30 degree/sec around the sample holder ϕ-axis and rocking at 10 degree/sec around the sample holder χ-axis, counting time : 15 min. Diffraction patterns from three points in the heated and unheated tusk dentin plates were obtained and averaged. The diffraction patterns were analyzed by JADE software.

FTIR was carried out using a HORIBA FT-530 micro-FTIR under the following conditions : detector : 16× MCT with LN_2 cooling, measuring area : 10μm × 10—50μm depending on the sample condition, resolution : 4cm^{-1}, scanning : 20 cycles, gain : auto, function : H-G. The obtained raw reflection spectrum was transformed into pseudo-transferred absorption pattern by the K-K function.

Results

Table 1 lists the color change of the heated tusk dentin. Below 400℃, the tusk dentin showed no color change and a natural white color. Above 500℃ the color changed to sooty gray. Above 700℃ the color faded to brownish, and then above 900℃ the color became white again.

The TG-DTA curve showed coupled strong exotherms from 300℃ to 500℃ and a weak exotherm at about 700℃, except for a broad endotherm with a weight loss of 16% below 200℃ attributed to

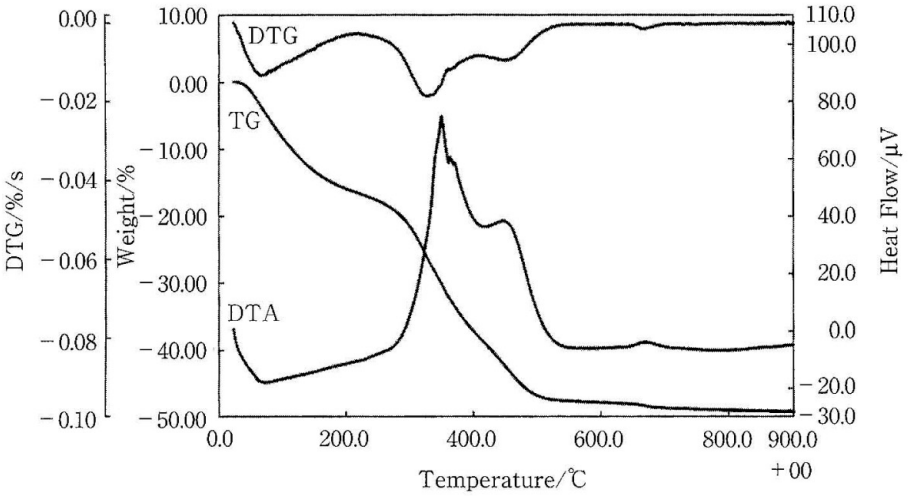

Fig. 1 TG-DTA curves of the mammoth dentin

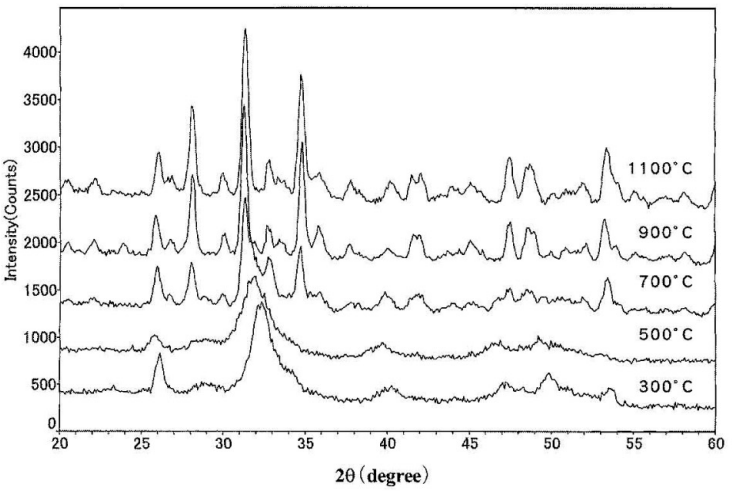

Fig. 2 XRD patterns of the mammoth dentin, after 300℃, 500℃, 700℃, 900℃ and 1,100℃ heating, from bottom to top, respectively.
Each pattern was shifted in order to make it legible.

dehydration (Fig. 1). The weight loss was about 21 wt% from 200℃ to 400℃, 11 wt% from 400℃ to 600℃, 1 wt% from 600℃ to 800℃, and less than 0.2 wt% from 800℃ to 1200℃ (Table 1).

The XRD patterns at 300℃, 500℃, 700℃, 900℃ and 1,100℃ are shown in Fig. 2. The other XRD patterns were a transition pattern between both ends. At 300℃ or below, the XRD pattern was a low crystalline apatite, typical of biological apatites. At 400℃ and above, the broad peak maximum shifted to the lower angles located among peaks of apatite and tricalcium phosphate. Above 700℃, a crystalline β-tricalcium phosphate phase, β-TCP, occurred in stead of apatite. Above 800℃, β-TCP was the only crystalline phase and the calculated unit cell dimensions were a = 10.359 Å and c = 37.21 Å, at the middle point of values for calcium phosphate and calcium-magnesium phosphate (Table 2).

Table 1 Results of TG, XRD, FTIR and colors after the heating treatments *

		TG	XRD			FTIR	
Sample	Color	Wt loss % in TG	HA	Intm	TCP	Organic	Inorganic
r.t.	Natural	–	Low XL	–	–	+ +	Ap
100 ℃	Natural		Low XL	–	–	+ +	Ap
200 ℃	Natural	16	Low XL	–	–	Start decay	Ap
300 ℃	Natural		Low XL	–	–	Decaying	Ap
400 ℃	Natural	21	Low XL	–	–	Weaken & broaden	Ap
500 ℃	Sooty gray			Low XL	–		Intm
600 ℃	Brownish	11	–	Low XL	–		Intm
700 ℃	Brownish		–	–	Low XL		TCP
800 ℃	White	1	–	–	XL		TCP
900 ℃	White		–	–	XL		TCP
1,000 ℃	White	< 0.2	–	–	XL		TCP
1,100 ℃	White		–	–	XL		TCP
1,200 ℃	White	< 0.1	–	–	XL		TCP

* : Low XL : low crystalline, XL : well crystalline, Ap : apatite, Intm : intermediate, TCP : β-tricalcium phosphate.

Heating treatment was carried out using a RIGAKU laser-furnace thermogravimetric-differential thermal analyzer, TG-DTA. The samples were heated to the set-up temperatures, 100℃ interval between 100℃ and 1,100℃, with an ascending rate of 5℃/min in a static atmosphere. The heating was quickly stopped when the sample reached the set-up temperature and rapidly cooled to room temperature using an air blow system.

X-ray diffraction (XRD) data was obtained by a RIGAKU-PSPC, position-sensitive-proportional-counter micro-XRD system under the following conditions : X-ray generator : rotary type Cu target, accelerating voltage : 50kV, current : 300 mA, X-ray beam collimeter : 30 μm, sample position : 10 degree to the incident beam, sample movement : rotation at 30 degree/sec around the sample holder ϕ-axis and rocking at 10 degree/sec around the sample holder χ-axis, counting time : 15 min. Diffraction patterns from three points in the heated and unheated tusk dentin plates were obtained and averaged. The diffraction patterns were analyzed by JADE software.

FTIR was carried out using a HORIBA FT-530 micro-FTIR under the following conditions : detector : 16× MCT with LN_2 cooling, measuring area : 10μm × 10—50μm depending on the sample condition, resolution : 4cm^{-1}, scanning : 20 cycles, gain : auto, function : H-G. The obtained raw reflection spectrum was transformed into pseudo-transferred absorption pattern by the K-K function.

Results

Table 1 lists the color change of the heated tusk dentin. Below 400℃, the tusk dentin showed no color change and a natural white color. Above 500℃ the color changed to sooty gray. Above 700℃ the color faded to brownish, and then above 900℃ the color became white again.

The TG-DTA curve showed coupled strong exotherms from 300℃ to 500℃ and a weak exotherm at about 700℃, except for a broad endotherm with a weight loss of 16% below 200℃ attributed to

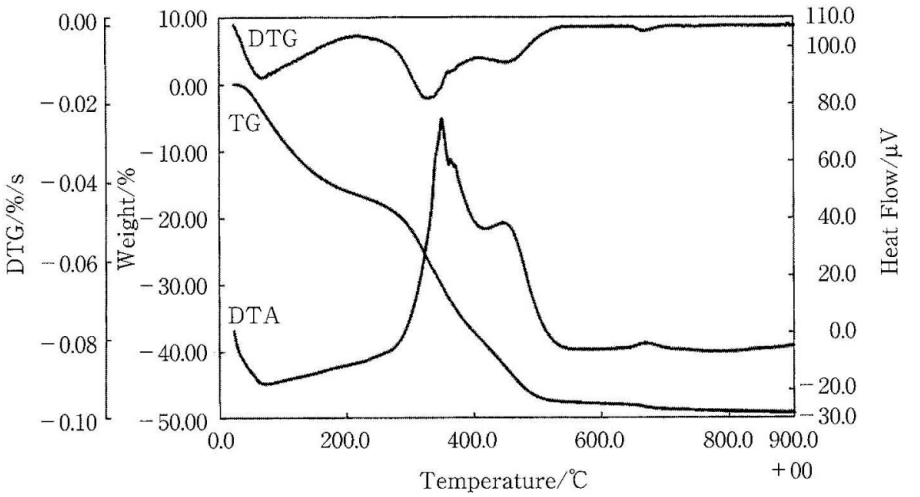

Fig. 1 TG-DTA curves of the mammoth dentin

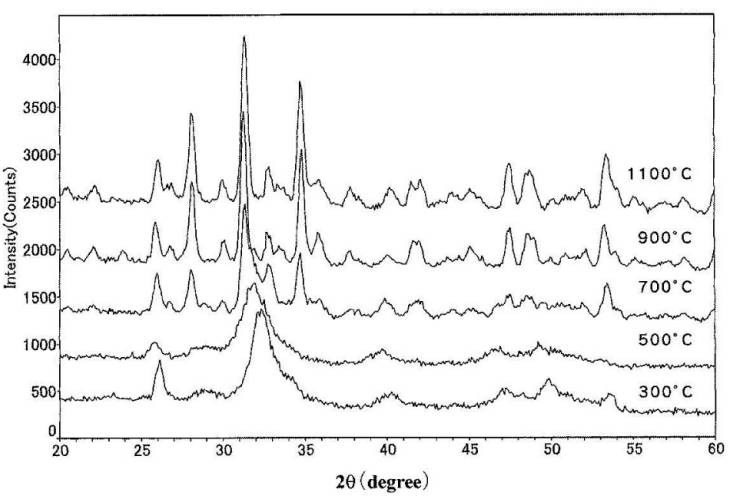

Fig. 2 XRD patterns of the mammoth dentin, after 300℃, 500℃, 700℃, 900℃ and 1,100℃ heating, from bottom to top, respectively.
Each pattern was shifted in order to make it legible.

dehydration (Fig. 1). The weight loss was about 21 wt% from 200℃ to 400℃, 11 wt% from 400℃ to 600℃, 1 wt% from 600℃ to 800℃, and less than 0.2 wt% from 800℃ to 1200℃ (Table 1).

The XRD patterns at 300℃, 500℃, 700℃, 900℃ and 1,100℃ are shown in Fig. 2. The other XRD patterns were a transition pattern between both ends. At 300℃ or below, the XRD pattern was a low crystalline apatite, typical of biological apatites. At 400℃ and above, the broad peak maximum shifted to the lower angles located among peaks of apatite and tricalcium phosphate. Above 700℃, a crystalline β-tricalcium phosphate phase, β-TCP, occurred in stead of apatite. Above 800℃, β-TCP was the only crystalline phase and the calculated unit cell dimensions were a = 10.359 Å and c = 37.21 Å, at the middle point of values for calcium phosphate and calcium-magnesium phosphate (Table 2).

Table 2 Unit cell dimensions of the heat-producted TCP

				PDF[18] card no.
Whitlockite (syn)	$Ca_3(PO_4)_2$	10.4290	37.3800	9-169
Mammoth dentin	After Heated at 1,200 ℃	10.359 (0.004) *	37.21 (0.01)	
Ca-Mg-Phosphate	$Ca_{2.81}Mg_{0.19}(PO_4)_2$	10.3370	37.0680	70-682

*: Figures in the parenthesis are the estimated standard deviations calculated by JADE software.

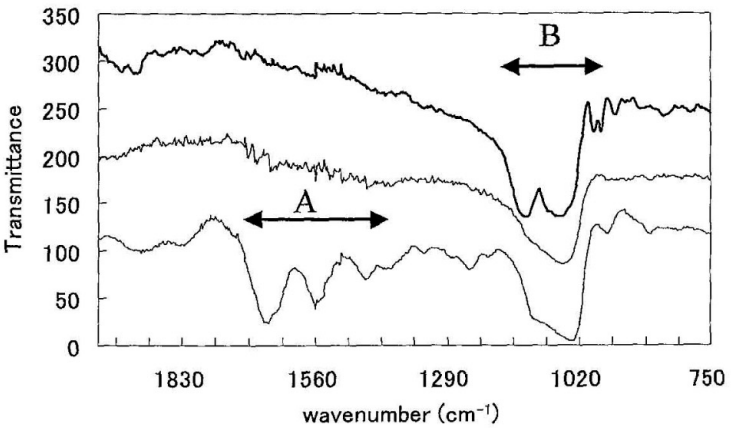

Fig. 3 FTIR spectra of the mammoth dentin, before the heating and after heating at 500℃ and 1,200℃, from bottom to top, respectively. A : Absorption due to amid, B : Absorption due to phosphate ions. The absorption at 964 cm^{-1} in the unheated sample was attributed to v1 of hydroxyapatite (ref.). Each pattern was shifted in order to make it legible.

Figure 3 shows the results of the FTIR study. These showed a correlation to a the organic and inorganic changes during heating, i.e., the organic compounds started to decay after 300℃, and completely combusted after 500℃, which was the temperature of the intermediate phase in the exchange to apatite (Table 1).

Discussion

The TG-DTA curve showed a large exotherm from 300℃ to 500℃ and a weak exotherm at about 700℃ corresponding to weight losses. The former exotherm was assumed to be due to combustion of dentin organic matrix[6-12], but the direct evidence had not been shown before. In this study TG-DTA analysis was coupled with FTIR and it was clearly shown that the absorption bands assigned to the organic composition diminished in the temperature range of 200℃ to 600℃ in accordance with the TG-DTA data. An organic content of about 32% in the mammoth dentin was comparable to the earlier report[7] and apparently larger than the value of about 20% for humans[10]. The reason for the high content of organic materials in mammoth tusk was not shown here, but it might be related to the size of tooth, because of the fact that the larger the tooth the higher the organic content[9,12].

Based on the XRD and FTIR data, the weak exotherm at about 700℃ indicated the crystalline phase transformation to crystalline β-TCP. This is harmony with the result of Lim and Liboff[5], who analyzed human dentin using a thermogravimeter, and concluded that between 700℃ and 800℃ apatite transformed into β-TCP.

In this study the apparent peak-shift found in the XRD pattern, and the broadened absorption in FTIR after 600℃ and 700℃ were attributed to the intermediate phase of the transformation from low crystalline apatite to the crystalline β-TCP. It has not been reported that the apatite crystal structure makes a solid-solution with tricalcium phosphate structure, while the apatite structure has the potential to include a wide variety of ionic substitutions[19,20]. The properties of the intermediate phase remained unclear and should be studied because the phase may play an important role in inorganic phase transformation.

This study highlighted a relation between organic combustion and the transformations of the crystalline phase. Collagen in dentin is tightly bonded to apatite as shown by Sakae, *et al.*[10]. They demonstrated the change in thermal behavior of collagen in mineralized and chemically de-mineralized dentin. In this study, FTIR results showed a crystalline phase transformation occurred with the diminishment of organic components, mainly collagen, by heating. This phenomenon is explained by the close relationship between the organic and inorganic components in dentin.

β-TCP in this study showed unit cell dimensions at the middle point of the values for calcium phosphate and calcium-magnesium phosphate. The unit cell dimensions usually reflect the chemical composition and ionic substitutions in a linear relationship[21], and therefore the roughly assumed chemical composition for the heat-producted β-TCP was $Ca_{2.81}Mg_{0.19}(PO_4)_2$ according to the estimation calculation known as Vegard's law[19] i.e. the unit cell dimensions correlate to the ratio of compositions which share the same atomic positions. For example, the a-axis dimension of the $(Ca, Mg)_3(PO_4)$ was written as $a = a(Ca_3(PO_4)_2) \cdot f(Ca_3(PO_4)_2) + a(Mg_3(PO_4)_3) \cdot f(Mg_3(PO_4)_3)$, where f is the fraction of the component.

The high concentration of Mg in the dentin might explain the rapid apatite diminishment by heating, unlike in human and bovine dentin, where the apatite phase remains after heating to 1,000℃ and higher[22,23]. In the comparative study of some animal dentin[9,10], there was a relationship between the magnesium content and the amount of the heat-product whitlockite. These studies showed that Probosidean dentin had a relatively large amount of magnesium, and that the formation of whitlockite in these dentin was at a lower temperature and had a larger volume after heating. These studies indicated that magnesium in dentin was a key trigger material that accelerates the thermal decomposition and transformation of dentin apatite into whitlockite.

Acknowledgements

The XRD instruments used in this study belong to the Laboratory for Electron Beam Research and Application (LEBRA), Institute of Quantum Science, Nihon University. Expenses was covered by the Frontier Science Project at LEBRA, 2001-2005, Nihon University. The authors thank Prof. I. Sato and the staff at LEBRA for their helpful discussion.

References

1) Robinson, C., Connell, S., Kirkham, J., Brooks, S.J., Shore R.C. and Smith, A.M. : The effect of fluoride on the developing tooth. Caries Res. **38** : 268—276, 2004.
2) Kameyama, A., Ihara, S., Amagai, T., Miake, Y., Kawada, E., Oda, Y., Yanagisawa, T. and Hirai, Y. : Adhesion of 4-META/MMA-TBB resin to heated dentin : effects of pre-treatments with $FeCl_3$ and/or HEMA. Dent. Mater. J. **22** : 1—9, 2003.
3) Fried, D., Zuerlein, M.J., Le, C.Q. and Featherstone, J.D. : Thermal and chemical modification of dentin by 9—11-μm CO_2 laser pulses of 5-100-μs duration. Lasers Surg. Med. **31** : 275—282, 2002.

4) Brauer, G.M., Termini, D.J. and Burns, C.L. : Characterization of components of dental materials and components of tooth structure by differential thermal analysis. J. Dent. Res. **49** : 100—110, 1970.
5) Lim, J.J. and Liboff, A.R. : Thermogravimetric analysis of dentin. J. Dent. Res. **51** : 509—514, 1972.
6) Sakae, T., Mishima, H. and Kozawa, Y. : Changes in bovine dentin mineral with sodium hypochlorite treatment. J. Dent. Res. **67** : 1229—1234, 1988.
7) Sakae, T., Akaishi, S., Mishima, H. and Kozawa, Y. : Thermogravimetric and differential thermal analysis of elephant tusk dentin. Nihon Univ. J. Oral Sci. **18** : 655—659, 1992. (in Japanese)
8) Larmas, M.A., Hayrynen, H. and Lajunen, L.H. : Thermogravimetric studies on sound and carious human enamel and dentin as well as hydroxyapatite. Scand. J. Dent. Res. **101** : 185—191, 1993.
9) Sakae, T., Mishima, H., Takahashi-Kunuki, Y., Suzuki, K. and Kozawa, Y. : Dentin apatites from teeth of different animals : crystallographic properties. Bull. de l' Institut Oceanographique, Monaco, n° Special **14** : 215—219, 1994.
10) Sakae, T., Mishima, H., Kozawa, Y. and LeGeros, R.Z. : Thermal stability of mineralized and demineralized dentin : a differential scanning calorimetric study. Connect. Tissue Res. **33** : 193—196, 1995.
11) Sakae, T., Yanaka, S., Watanabe, H. and Kozawa, Y. : Formation of porous and dense calcium phosphate structure by cintering of dentin. Nihon Univ. J. Oral Sci. **22** : 45—51, 1996. (in Japanese)
12) Sakae, T. : Toothed whale dentin collagen studied with thermal analysis technique. In : Biomineralization and hard tissue of marine organisms. (eds. Wada, K. and Kobayashi, S), pp. 143—149, Tokai Univ. Press, Tokyo, 1996. (in Japanese)
13) Bachmann, L., Thome Sena, E., Fernando Stolf, S. and Maria Zezell, D. : Dental discolouration after thermal treatment. Arch. Oral Biol. **49** : 233—238, 2004.
14) Rowles, S.L. : Chemistry of the mineral phase of dentin. In : Structural and chemical organization of teeth. (ed. Miles, A.E.W.), pp. 201—246, Academic Press, New York, 1967.
15) Schaedler, J.M., Krook, L., Wootton, J.A., Hover, B., Brodsky, B., Naresh, M.D., Gillette, D.D., Madsen, D.B., Horne, R.H. and Minor, R.R. : Studies of collagen in bone and dentin matrix of a Columbian mammoth (late Pleistocene) of central Utah. Matrix **12** : 297—307, 1992.
16) Raubenheimer, E.J., Brown, J.M., Rama, D.B., Dreyer, M.J., Smith, P.D. and Dauth, J. : Geographical variations in the composition of ivory of the African elephant (*Loxodonta africana*). Arch. Oral Biol. **43** : 641—647, 1998.
17) Raubenheimer, E.J., Bosman, M.C., Vorster, R. and Noffke, C.E. : Histogenesis of the chequered pattern of ivory of the African elephant (*Loxodonta africana*). Arch. Oral Biol. **43** : 969—977, 1998.
18) Powder Diffraction File (PDF) : International Centre for Diffraction Data, Pennsylvania, USA, card no. 9—169 and no. 70—682, 2000.
19) McConnel, D. : Apatite. pp. 22—32, Springer-Verlag, New York, 1973.
20) Elliott, J.C. : Structure and Chemistry of the Apatites and Other Calcium Orthophosphates. pp. 111—190, Elsevier, Amsterdam, 1994.
21) LeGeros, R.Z. : Calcium Phosphates in Oral Biology and Medicine. pp. 82—107, Karger, Basel, 1991.
22) Dickens, B., Schroeder, L.W. and Brown, W.E. : Crystallographic studies of the role of Mg as a stabilizing impurity in β-$Ca_3(PO_4)_2$. I. The crystal structure of pure β-$Ca_3(PO_4)_2$. J. Solid State Chem. **10** : 232—248, 1974.
23) Sakae, T., Mishima, H., Kozawa, Y., Yamamoto, H., Nagano, E. and Hirai, G. : Thermal study of the formation of magnesium whitlockite from hydroxyapatite and magnesium phosphate. Nihon Univ. J. Oral Sci. **14** : 463—468, 1988. (in Japanese)

Int J Oral-Med Sci 2(1):23-32, 2004

Original Article

A Morphological Study of Biomimetic Approach for Pathological Calcification *In Vitro*

Emiko Matsumura

Nihon University Graduate School of Dentistry at Mastudo, Oral Pathology, Matsudo, Chiba 271-8587, Japan

Correspondence to: Emiko Matsumura
E-mail: matumura@mascat.nihon-u.ac.jp

Key words:
pathological calcification, biomimetic approach, simulated body fluid, physicochemical factor, calcium phosphate

Abstract

Pathological calcification is included in disorders such as arteriosclerosis, circulatory failure of the heart valves, and renal failure and many studies have been performed to elucidate the development mechanism of pathological calcification. In this study, it has been carried out the observation of pathological calcification using simulated body fluid (SBF) under biomimetic approach. The aim of this study was to understand the mechanism of calcification in biological tissues. The porcine heart, aortic valve and small intestine were used in this study. The solutions for this study were prepared to suspend those specimens such as SBF pH 7.4, pH 5.0, supplemented with Mg, supplemented with CO_3, porcine serum (PS) and saline solution. The specimens were suspended and were kept at 37 °C in an incubator. After 7 and 14 days, they were analyzed using scanning electron microscopy (SEM) and energy dispersive X-ray spectroscope detector (EDS). The deposits that had crystal-like structure were observed in SEM from those specimens after 7 days, and some of them showed high peak of calcium and phosphate by EDS. They were roughly classified into five types based on the shape. This study suggested that calcified deposits on biological tissue *in vitro* in this biomimetic approach were affected with physicochemical factors such as Mg, CO_3 and pH. This biomimetic approach would contribute to understand the mechanism of pathological calcification. Moreover, it showed that calcified deposit could be formed *in vitro* without cell involvement in the solution.

Introduction

Vascular calcification is considered to be associated with disorders such as atherosclerosis, circulatory failure of the heart valves and renal failure, and many studies have been performed to elucidate the development mechanism of pathological calcification. The mechanism of calcification is basically considered to be active and passive processes. Anderson suggested mineral phase in initiation of pathologic calcification in association with the action of cellular membrane (1). On the other hand, Schinke *et al.* (2) reported a passive process, in which was supported that physicochemical factor was regarded to play important role to calcification (3). There have been a variety of morphological and physicochemical studies in the calcification and calcified deposition in advanced arteriosclerosis (4), dental (5) and salivary calculus (6), cardiovascular calcified deposition (7), and vascular calcification in chronic renal failure (8) has been reported.

Vascular calcification is considered to be mostly consisted of calcium phosphate crystal and chemical analyses of calcified deposits are important clues for investigation of the details of the cause of vascular calcification (7-12). Although earlier calcified deposition mechanism has not yet been clarified, it is considered that nuclear formation and its chemical synthesis have great influence on the formation of calcified deposits in most cases, and the formation progresses through the derivation and growth of precursors of the constituents (10). The initial step of vascular calcification is considered to start with formation of one or more unstable apatite precursors, amorphous calcium phosphate, or octacalcium phosphate (3, 13).

Analyses of morphology and the chemical components of the crystals and deposits by scanning electron microscope (SEM) and energy dispersive X-ray spectroscope detector (EDS) may be important clues for investigation of characteristic crystals and deposits (5-7). Using these instruments, crystallographic investigation of the morphology and chemical components of calcification have

been carried out on dental calculus by Sakae *et al.* (5) and human salivary calculus by Mishima *et al.* (6). To demonstrate the findings of these in vivo morphological studies, many experimental pathological studies using *in vitro* vascular calcification models have been performed (9, 14).

Biomimetics means imitation of the body (nature), and is a new concept that has been introduced (15, 16). Examples include ceramics and implant coating agents under conditions imitating the biological environment using simulated body fluid. This simulated body fluid was developed and standardized by Kokubo *et al.* (17) and has frequently been used in the last decade in biomimetic approach to measure the affinity of biomaterials by observing the formation of bone-like apatite on the surface of the biomaterial as an indicator of the biocompatibility of the biomaterial. Since no biomimetic study has been reported with biological tissue such as the porcine heart, aortic heart valve and small intestine previously, the author performed this experimental pathological investigation of vascular calcification *in vitro* using biomimetic approach.

Materials and Methods

Biological samples

The porcine aortic valve, heart, and small intestine were purchased from a slaughterhouse in New York, USA. The total of three porcinis was used to this study. Four specimens were cut from one porcine. Each two specimens were cut from the rest two porcines, respectively. Eight specimens were totally used in this study. The specimens were rinsed well with saline solution, and the heart was cut into 1cm square pieces, and the aortic valve and small intestine were cut into 5 mm circular slices.

Suspension solutions

To suspend the tissues, three types of solution, simulated body fluid (SBF), porcine serum (PS), and saline solution as a control, were prepared. The ion concentrations in SBF are shown in Table 1 (17). These solutions were further classified. As SBF, solutions at pH 7.4 and 5.0 and solutions with 10% weight increased magnesium and carbonate designated as SBF with Mg and SBF with CO_3 were prepared for observation of morphological changes. As for PS, solutions at pH 7.4 and 5.0 were prepared. A total of seven types of solution for suspension shown below were prepared.

(1) SBF pH 7.4
(2) SBF pH 5.0
(3) SBF with Mg (pH 7.4)
(4) SBF with CO_3 (pH 7.4)
(5) PS pH 7.4
(6) PS pH 5.0
(7) Control (saline solution)

Table 1. Composition of simulated body fluid (SBF)

Reagents	Solutions		
	SBF	SBF with Mg	SBF with CO_3
$MgCl_2 \cdot 6H_2O$	0.3048 g/ 500 ml	0.3088 g/ 500 ml	0.3048 g/ 500 ml
$CaCl_2$	0.2774	0.2774	0.2774
Na2SO4	0.0710	0.0710	0.0710
$NaHCO_3$	0.1890f	0.1890	0.1890
$K2HPO_4 \cdot H_2O$	0.1922	0.1922	0.1922
NaCl	8.0063	8.0063	8.0063
KCl	0.2236	0.2236	0.2236
pH	7.4, 5.0	7.4	7.4

SBF pH5.0 was adjusted with 0.1M HCl. The ion concentration (mM) of SBF: Na^+, 142.0; K^+, 5.0; Mg^{2+}, 1.5; Ca^{2+}, 2.5; Cl^-, 148.8; HCO_3^-, 4.2; HPO_4^{2-}, 1.0; SO_4^{2-}, 0.5

Suspension experiment

The three types of tissue were suspended in the seven types of solution in an incubator at 37°C, each solution was changed every day during the suspension with 0.2% thymol solution. This solution was added to avoid getting bacteria. The surfaces were observed on days 7 and 14 using SEM and EDS.

SEM analysis

The SEM used for observation of the morphology and size of surface deposits was a JEOL JSM 5400, Tokyo, Japan with an accelerating voltage of 20kV and working distance of 15mm. The suspended materials were transferred to fixative. The fixative solution was prepared as follows: 17.6 ml of 1 M sodium monophosphate (pH 8.9) and 60.8 ml of 0.2 M potassium monophosphate (pH 4.4) were mixed. It was adjusted to pH 7.4 using 0.1M HCl. 50 ml of this mixture, 12 ml of 0.75 M glutaraldehyde solution and 38 ml of distilled water were combined, and used as the fixative solution.

The materials were suspended in 10 ml of the fixative solution for 5 minutes. Then, the fixative solution was changed to the new fixative solution, and the materials were kept at room temperature for one hour. After one hour, the fixative solution was removed, and the materials were sequentially dehydrated in 10 ml of 70, 80, 90, and 100% ethanol for 20 minutes each. The materials were completely dried using a critical point drying apparatus (Enton Accum, Inc.), and coated with carbon.

EDS analysis

EDS (Evex microanalysis MODEL 500) connected to a SEM was used to investigate the components of the deposits in the following condition: X-title angle, 40 ° ; counting time about 300 seconds. About 10 points were analyzed on each specimen.

Results

Morphological observation under SEM

Table 2 represents the amount (number) of deposits having crystal-like structure on the surface of the tissues. The deposit was compared with the smooth surface in the specimen from the control. Deposits were noted in all tissues. The amount of deposits was high in the samples treated with SBF with Mg and SBF with CO_3.

Results of EDS analyses

EDS analyzed the components of the deposits observed by SEM. The results are shown in Table 3. In Table 3, the deposits are classified based on the presence or absence of the major calcification component, calcium and phosphate. The deposits observed by SEM were divided into calcified deposits associated with calcification and deposits unrelated to calcification.

Table 2. Amount of the deposits on surface

Sample	Solution						
	SBF pH 7.4	SBF pH 5.0	SBF with Mg	SBF with CO_3	PS pH7.4	PS pH 5.0	Control (Saline solution)
Heart	++	++	+++	++	+	+	+
Aortic valve	++	++	+++	+++	+	+	+
Intestine	+	+	+++	+++	+	+	+

+: represents the presence of a few deposits on the surface
++: represents more deposits than +
+++: represents many deposits covering up the surface in some regions†

Table 3. Existence of calcium phosphate in the deposits

Sample	Solution						
	SBF pH7.4	SBF pH5.0	SBF with Mg	SBF with CO_3	PS pH7.4	PS pH5.0	Control (Saline solution)
Heart	○	○	○	○	○	×	×
Aortic valve	○	○	○	○	○	×	×
Intestine	○	○	○	○	×	×	×

○ : represents calcium phosphate in the deposit
× : represents no calcium phosphate in the deposit

Classification by morphology and tissues

Calcified deposits with various morphological features were noted on the surfaces of the samples treated with the various solutions by SEM and EDS (Tables 2 and 3) confirmed these calcified deposits to mainly contain calcium and phosphate.

The calcified deposits were roughly classified into five types, A, M, P, R and N based on the shape. The five types had the following morphological characteristics such as shape and size under SEM. Amorphous shape type (A): deposits had irregular shapes formed with round and sharp lines and covered up a part of the surface. Most of the surface looked smooth at high magnification (Figs. 1, 2). Massive shape type (M): deposits had small and large granular to massive shapes. these showed rough at high magnification (Fig. 3). Plate shape type (P): deposits appeared flat on the surface, the surface showed basically smooth at high magnification (Fig. 4). Round shape type (R): several individual spherical deposits were present on the smooth surface (Fig. 5). Non-specific shape type (N): deposits had shapes difficult to be classified into the above types and deposits with mixed types of shape. (Figs. 6-8)

The distributions of the above types in the solutions and tissues are shown in Table 4. The results of the EDS are shown in Fig. 9, 10. SEM findings of calcified deposits demonstrated to contain calcium phosphate by EDS are shown below (Table 3). The peak of EDS in this study showed varieties pattern to each specimen.

Results of the experiment using SBF pH 7.4

A and M types were formed in the aortic valve. M type deposits were far dominant in quantity than A type. The shape and location varied among the M type deposits, and the deposits consisted of small and large various shapes. A and M types were also observed in the heart, and the M type deposits were predominantly larger than the A type deposits. The size of deposits was slightly different between the deposits in the aortic valve and heart, and the deposits were slightly larger in the aortic valve than in the heart. In the small intestine, only M type was noted, and various large and small shapes formed with curves and uneven lines were observed. Deposits in the small intestine were fewer than that in the aortic valve and heart by SEM.

Results of the experiment using SBF pH 5.0

A, M and N types were formed in the aortic valve. The morphology of the N type deposits in the aortic valve was specific to this solution. A and M types were formed in the heart, and there were more diminutive granular M type calcified deposits over the surface than A type. In the small intestine, A, M and N types were observed as in the aortic valve, and the deposits had similar morphology, but no identical morphology was noted.

Results of the experiment using SBF with Mg

In the experiment using SBF with Mg, various types were observed in all tissues compared to the other solutions. A and M types were formed in the aortic valve, and P type was additionally seen in the heart. Moreover, various deposits of all types, A, M, P, R, and N types, were formed in the small intestine.

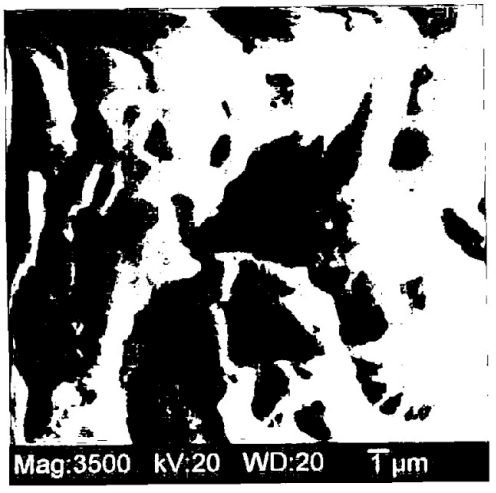

Fig. 1. A type: The deposits contain many layers of calcium phosphate from SBF with Mg in an intestinal sample.

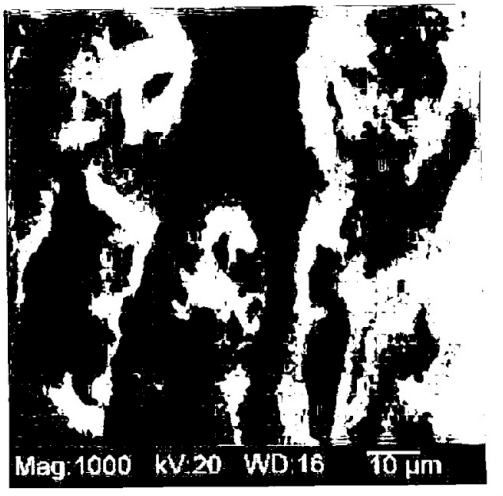

Fig. 2. A type: The surface is rough and irregular from SBF with CO3 in an aortic valve sample.

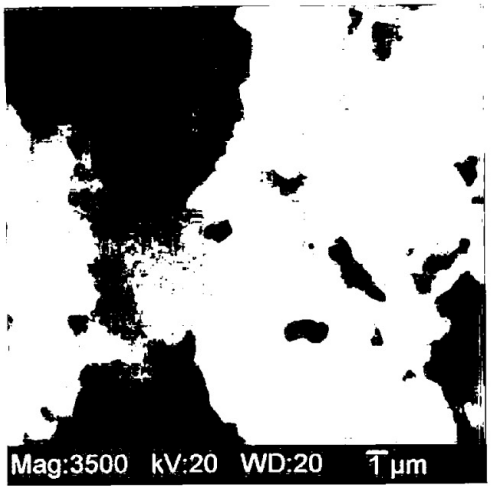

Fig. 3. M type: The deposit is composed of many small granulates on the smooth surface from SBF with Mg in an aortic valve sample.

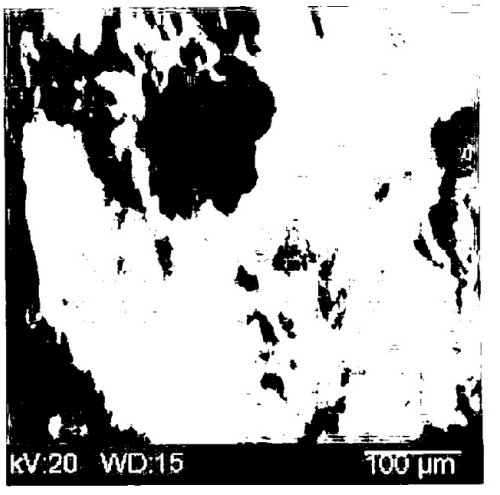

Fig. 4. P type: A part of the deposit with flat shape from SBF with Mg in an aortic valve sample.

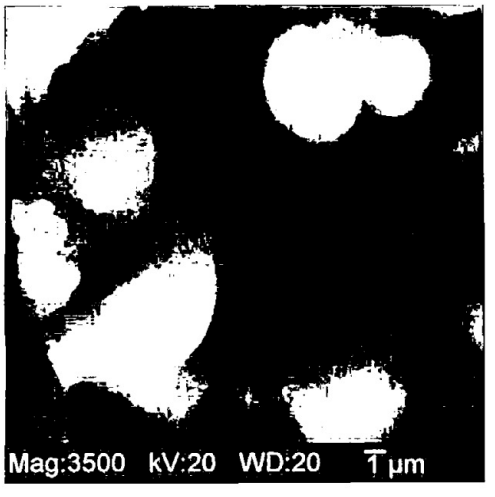

Fig. 5. R type: Several spherical deposits on the surface from SBF with Mg in an intestinal sample.

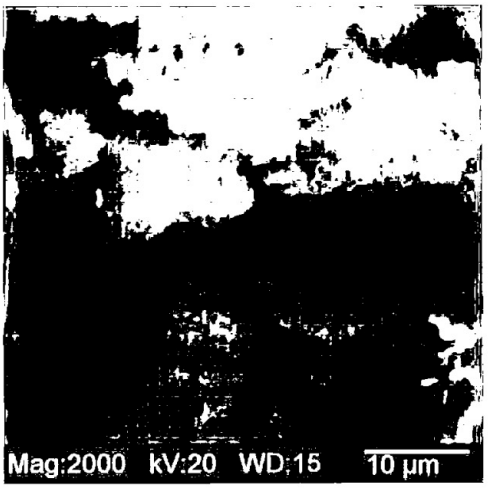

Fig. 6. N type: Combination of massive and plate deposits from SBF with CO3 in an intestinal sample.

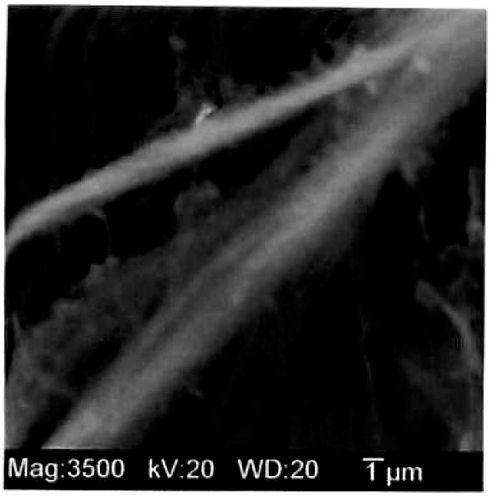

Fig. 7. N type; Several rod deposits on the surface from SBF pH5.0 in an aortic valve sample.

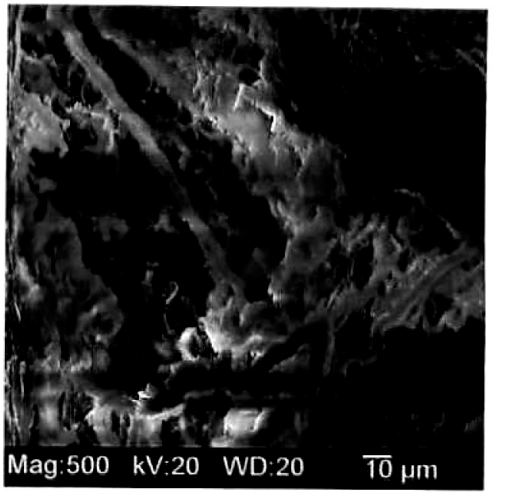

Fig. 8. N type; The deposit is composed of different types of shape, such as rod and granulates from SBF pH5.0 in an intestinal sample.

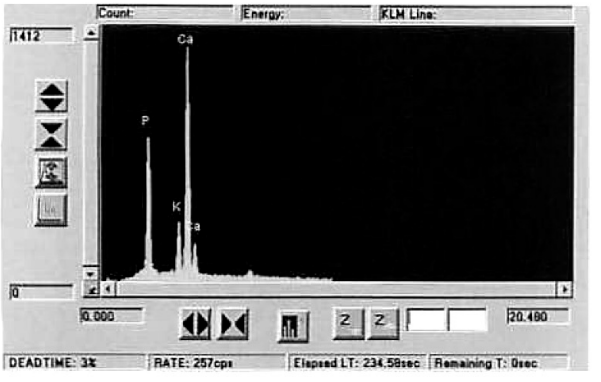

Fig. 9. EDS shows calcium phosphate from SBF with CO_3 in a heart sample.

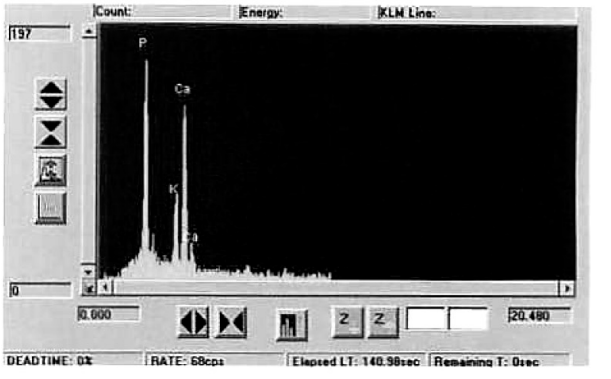

Fig. 10. EDS shows calcium phosphate from SBF pH7.4 in an aortic valve sample.

Results of the experiment using SBF with CO_3

A, M, N, and P types were observed in the aortic valve. Surface calcified deposits were slightly increased on day 14 compared to those on day 7. In the heart, only M type was noted with various sizes. The outward appearance of the deposits was slightly more round on day 14 than on day 7. In the small intestine, the calcified deposits covering up the surface consisted of M and N types: with various shapes such as irregular rods shape, droplet shape, and round shape.

Results of the experiment using PS pH 7.4

A and M types were formed in the aortic valve, and the surface was widely covered with A type deposits with unclear outward appearance. M and N types were noted in the heart, and these calcified deposits were far fewer than those formed in the other solutions. Some M type calcified deposits had characteristic morphology, diminutive granular deposits on the surface in large clusters. In the small intestine, EDS did not detect materials appearing calcium phosphate as SEM observed deposits.

Results of experiment using PS pH 5.0

Although surface deposits were noted under a SEM in all tissue samples, EDS did not demonstrate the presence of calcium phosphate.

Results of experiment using control

The surface was basically smooth in the samples treated with the control, however, a very low amount of calcium phosphate was detected with many chemical substances only in one deposit in the aortic valve.

Table 4. Classification of the crystal types based on the shape

Sample	Solution						
	SBF pH7.4	SBF pH5.0	SBF with Mg	SBF with CO_3	PS pH7.4	PS pH5.0	Control (Saline solution)
Heart	M,A	M,A	M,A,P	M	A	–	–
Aortic valve	M,A	M,A,N	M,A	M,A,P	A,M	–	–
Intestine	M	M,A	M,A,N,P,R	M	–	–	–

SBF: simulated body fluid solution, PS: porcine serum,
Type of crystal shape; A: amorphous type, M: massive type, P: plate shape type R: round shape type, N: non-specific type,

Discussion

Calcification in arteriosclerosis, artificial heart valves, salivary calculus, and dental calculus has been investigated by SEM, Fourier transform infrared spectroscope detector, X-ray diffraction, and crystal imaging analysis using EDS, and the major chemical component have been determined to be calcium phosphate (3, 5-8, 18, 19). Some deposits onthe surfaces of the tissues observed by SEM were demonstrated to be calcified deposits containing calcium phosphate (Figs. 1-8). The distribution of calcified deposits in the solutions and tissues shown in Table 4. In the control, some deposits on the surfaces observed by SEM. However some surfaces had deposits that did not contain calcium and phosphate with EDS.

Calcium phosphate was detected with EDS, infrequently with other chemical components. EDS result showed the diminutive amount of calcium phosphate in the above deposit and its presence with other chemical components: usually calcium phosphate was detected alone or with a few other components as shown in Figs. 9 and 10, and it was suggested that calcium phosphate adhered or was formed due by some reasons. LeGeros (3) reported that presence of mixed calcium phosphate indicated changing condition of pH and composition in the biological fluid, which were normally supersaturated with respect to apatite. In this study, SBF was the biological fluid. In biological systems, apatite which forms is mainly carbonate apatite (CHA). CHA can readily precipitate when the supersaturation of the biological fluid in the microenvironment is exceeded. One of the means of exceeding supersaturation leading to the precipitation of CHA is the release of calcium ions into the microenvironment resulting from cell death(20). Thus, cell death from biological tissues in the present study could be nucleation for the calcified deposit. This finding supported the initiation of the pathological calcification.

The morphology of the calcified deposits was significantly different among the samples treated with the various solutions. Regarding the difference between the deposits formed in SBF and PS, as clarified by classification shown in Table 4, various types of calcified deposits were formed in SBF, while only a few types were formed in PS pH7.4. This difference was obvious on the morphological observation by SEM.

At a low magnification, many deposits were noted in the samples treated with SBF, however, and fewer deposits were observed in the samples treated with PS. The major difference in the composition between SBF and PS is that PS contains protein. Although protein is a component of calcification (19), serum may contain not only components that promote calcification but also components that inhibit calcification. As for differences due to pH, no major difference was observed in the morphological types shown in Table 4, but deposits formed in PS pH 7.4 and PS pH 5.0 were obviously different. In PS pH 5.0, the deposits were present on the tissue surface, but they did not contain calcium phosphate, suggesting that acidic environment is not appropriate for calcification. Although no major morphological difference was noted in the regions of

calcified deposition among the SBF, the detection rate of calcium phosphate by EDS was higher in PS pH 7.4 than in PS pH 5.0: calcium phosphate was detected in most deposits formed in PS pH 7.4. Therefore, pH of the solution may be involved in the amount (rate) of calcium phosphate production.

Major differences were observed in the deposits formed in modified SBF, SBF with Mg and SBF with CO_3. Regarding the morphological types, as shown in Table 2, a variety of morphology was observed in the deposits formed in SBF with Mg. Similar results were obtained in the experiment using SBF with CO_3, particularly in the aortic valve. Okazaki *et al.* (21) investigated the influences of physicochemical factors on the morphology of calcified deposits, particularly on calcium phosphate, and suggested that addition of magnesium and carbonate changed the size and shape of calcium phosphate (3, 8). The findings of this study might have resulted from changes of type of the solution such as adding with Mg and CO_3.

There was no marked morphological difference among the calcified deposits in the aortic valve, heart, and small intestine in the classification shown in Table 4, suggesting that calcified deposition may occur in all organs in the experiments using SBF. The presence of bone-like apatite containing calcium phosphate has been demonstrated in studies of compatibility of biomaterials by keeping biomaterials in SBF (13, 22), but there has been no study using biological tissues. The size of individual deposits was greater in the aortic valve than in the other two organs. EDS detected a difference in the small intestine.

The calcified deposit which reviewed by EDS and SEM from this study will be useful to explain the mechanism of vascular calcification due to type of the solution and pH. Whether the mechanism of calcification is active or passive, it is still unclear. However, this study with biomimetic approach supported the passive process. LeGeros (23) reported that calcium phosphate, dicalcium phosphate dihydrate crystal (DCPD) was induced from the gel system. The shape of DCPD revealed spherical shape and was seen to form on the top of the layer in the solution. Their shape was similar to M type shape in this study. Therefore, the calcified deposit in this study was composed of calcium phosphate crystal.

The mechanism of calcification, especially vascular calcification is regarded to be "active or passive process" (24, 25). Proudfoot *et al.* (24) and Tintut *et al.* (26) supported active process through cell-mediated process. However, some studies reported that vascular calcification could be derived from physicochemical principles (3, 18). In this study, the physicochemical factors such as magnesium, carbonate and pH were used to induce calcified deposit. They were observed to have different type of shapes in the morphology with SEM and EDS. These results suggest that physicochemical factor would act to induce or change the morphology of calcified deposit without the involvement of cell. Therefore, the present study was identified as one of the passive process in pathological calcification.

Conclusion

Calcified deposits with various morphological features formed in biological tissues were obtained in an *in vitro* biomimetic approach. The morphology of the calcified deposits was affected by the physicochemical factors of type of the solution and pH.

This study suggested that the formation of calcified deposit might be involved to crystal-like structure, and this would be useful to know the characterization of calcified deposit through their growth. Since the morphology varied among the tissues, tissue specificity might be related. The above findings clarified that calcified deposition in the tissues *in vitro* was due to interaction between the type of the solution and tissue, and suggested the possibility of calcification without involvement of cells, which was intermediate between two calcification mechanisms, active and passive processes. These findings support the passive development mechanism, and may lead to elucidation of the causes of pathological calcification in arteriosclerosis, artificial heart valves, renal failure and salivary calculus.

The findings also demonstrated the usefulness of experiments using biomimetic approach. This approach could be possible to form the crystal-like structure that contained calcium phosphate at 7 days. This study developed the vascular calcification model *in vitro* with biological tissues such as the porcine heart, aortic valve and small intestine using biomimetic approach. Therefore, the results suggested that this study provided the evidence of the induction of calcified deposits without involvement of cells.

Acknowledgments

I deeply appreciate Professor Hirotsugu Yamamoto, Nihon University, School of Dentistry at Mastudo, Department of Pathology, for his sincere instruction and review, and Professor Racquel Zapanta LeGeros, New York University, College of Dentistry, Department of Biomaterial and Biomimetics, for her guidance of the experiments. I am thankful for Professors Furuyama, Kozawa and Ogata, Nihon University, School of Dentistry at Mastudo, to give great advice to this study. I also thank Professors John P LeGeros and Van Thompson, New York University, College of Dentistry, Department of Biomaterial and Biomimetics, for sharing the facility and support for the experiments. I also deeply appreciate Associate Professor Toshiro Sakae, Nihon University, School of Dentistry at Mastudo, Department of Anatomy II, and Lecture Hiroyuki Okada, Department of Pathology, for their help in proceeding in the study. I give specially thanks Mr. T. Matsumoto Nihon University, School of Dentistry at Mastudo, Dental Hospital, Department of Clinical cytology, to his technical help and great encouragement to my study. I also acknowledge Assistant, Dr. Sisilia F Fifita, Mrs. Miyuki Saito and the staff of Nihon University, School of Dentistry at Mastudo, Department of Pathology, for their help and support. I appreciate Dr. Masly Harsono, New York University, College of Dentistry, Department of Biomaterial and Biomimetics, to his advice to my study. Finally I'm deeply thankful for my parents and grandmother about their encouragement and love.

References

1. Anderson HC: Vesicles and calcification. Current Rheum Rep, 5:222-226, 2003.
2. Schinke T, Karsenty G: Vascular calcification; A passive process in need of inhibitors. Nephrol Dial Transplant, 15:1272-1274, 2000.
3. LeGeros RZ: Formation and transformation of calcium phosphates; relevance to vascular calcification. Z Kardiol, 90:116-124, 2001.
4. Matsumura E, Utsunomiya T, Sakae T, LeGeros RZ, Yamamoto H: A study of characteristic crystal in arteriosclerosis. Nihon Univ J Oral Sci 27:80-84, 2001.
5. Sakae T, Yamamoto H, Mishima H, Matsumoto T, Kozawa Y: Morphology and chemical composition of dental calculi mainly composed of whitlockite. Scanning Microsc. 3:855-860, 1989.
6. Mishima H, Yamamoto H, Sakae T: Scanning electron microscopy-energy dispersive spectroscopy and X-ray diffraction analyses of human salivary stones. Scanning Microsc, 6:487-494, 1992.
7. Tomazic BB, Brown WE, Schoen FJ: Physicochemical properties of calcific deposits isolated from porcine bioprosthetic heart valves removed from patients following 2-13 years function. J Biomed Mater Res, 28:35-47, 1994.
8. LeGeros RZ, Contiguglia SR, Alfrey AC: Pathological Calcifications Associated with Uremia; Two types of Calcium phosphate deposits. Calc Tiss Res, 13:173-185, 1973.
9. Tomazic BB, Chow LC, Carey CM, Shapiro AJ: An *in vitro* diffusion model for the study of calcification of bovine pericardium tissue. J Pharm Sci, 86:1432-1438, 1997.
10. Epple M, Lanzer P: How much interdisciplinary is required to understand vascular calcifications?; Formation of four basic principles of vascular calcificatio. Z Kardiol, 90:2-5, 2001.
11. Branko B, Tomazic BB, Edwards WD, Schoen FJ: Physicochemical characterization of natural and bioprosthetic heart valve calcific deposits: Implications for prevention. Ann Thorac Surg, 60:322-327, 1995.
12. Peters F, Epple M: Simulating arterial wall calcification *in vitro*: Biomimetic crystallization of calcium phosphates under controlled conditions. Z Kardiol, 90:81-85, 2001.
13. Tomazic BB, Siew C, Brown WE: A comparative study of bovine pericardium mineralization: A basic and practical approach. Cells Materials, 1:231-241, 1991.
14. Shioi A, Mori K, Wakikawa T, Hiura Y, Koyama H, Okuno Y, Nishizawa Y, Morii H: Mechanisms of atherosclerotic calcification. Z Kardio, 89:75-79, 2000.
15. Tanahashi M, Kokubo T, Matsuda T: Quantitative assessment of apatite formation via a biomimetic method using quarts crystal microbalance. J Biom Mater Res, 31:243-249, 1996.
16. Osada T, Kai M, Kakazu Y, Kataoka I, Sakai K, Tanaka J: Handbook of biomimetics, 2000, NTS Press, Tokyo, Japan.
17. Kokubo T, Kim HM, Kawashita M, Nakamura T: Process of calcification on artificial materials. Z Kardiol 90: 86- 91, 2001.
18. Tomazic BB: Physicochemical principles of cardiovascular calcification. Z Kardiol, 90:68- 80. 2001.
19. Schmid K, Mcsharry WO, Pameijer CH, Binette JP: Chemical and physicochemical studies on the mineral deposits of the human atherosclerotic aorta, Atherosclerosis, 37:199-210, 1980.
20. Proudfoot D, Schanahan CM, Weissberg PL: Vascular calcification: New insight into an old problem. J Pathol, 185:1-3, 1998.
21. Okazaki M, LeGeros RZ: Properties of heterogeneous apatites contatining magnesium, fluoride and carbonate. Adv Dent Res, 10: 252-259, 1996.
22. Mako WJ, Vesely I: *In vitro* and *In vivo* models of calcification in porcine aortic valve cusps. J Heart Valve Dis, 6:316-323, 1997.
23. LeGeros RZ: Calcium phosphate in oral biology and medicine. In: Myers HM, editor. Monographs in oral science, Basel: Karger; 1991. p. 62-65.

24. Proudfoot D, Skeepper JN, Shanahan CM, Weissberg PL: Calcification of human vascular cells *in vitro* is correlated with high levels of matrix Gla protein and low levels of osteopontin expression. Arterioscler Throm Vasc Biol, 18:379-388, 1998.
25. Christian RC, Fitzpatrick LA: Vascular calcification. Curr Opn Neph Hyper, 8:443-448, 1999.
26. Tintut Y, Dermer LL: Recent advances in multifactorial regulation of vascular calcification. Curr Opi Lip, 12:555-560, 2001.

Journal of Oral Rehabilitation 2004 **31**; 67–73

Calcium phosphate formation on the phosphorylated dental bonding agent in electrolyte solution

T. HAYAKAWA*, M. YOSHINARI†, T. SAKAE‡ & K. NEMOTO* *Department of Dental Materials, Research Institute of Oral Science, Nihon University School of Dentistry at Matsudo, †Department of Dental Materials Science and Oral Health Science Center, Tokyo Dental College, Mihamaku and ‡Department of Anatomy, Research Institute of Oral Science, Nihon University School of Dentistry at Matsudo, Matsudo, Japan

SUMMARY **The aim of the present study was to study the mineral formation on a phosphorylated dental bonding agent using a mineralization inductive solution. Clearfil Photobond, which contained phosphate monomer, was cured by photo-irradiation and heat treated, and was then immersed in Hanks' balanced salt solution (HBSS) with pH = 7·4 for 1, 3, 5, 7, 14, and 28 days at 37 °C. The white substances were deposited on the phosphorylated polymer, i.e. cured Photobond disk, after the immersion in HBSS. The white substances become visible after 3 days immersion. After 7 days immersion, surface of the phosphorylated polymer disk was almost covered with white substance layers. The measurement of white substances by means of X-ray diffraction, Fourier-transform infrared and electron probe microanalysis revealed that their main component was carbonate-containing hydroxyapatite. Scanning electron microscopy pictures showed that a large number of globules of hydroxyapatite were fused together, and that each globule was composed of a group of numerous thin-film form flakes uniting and/or clustering together. The results obtained in this study concluded that the presence of phosphonic acid and phosphate group of phosphorylated dental bonding agent enhanced the nucleation and growth of hydroxyapatite crystals on its surface.**

KEYWORDS: **calcium phosphate, electrolyte solution, phosphorylated dental bonding agent, methacryloxydecyl hydrogen phosphate, carbonate apatite, remineralization**

Introduction

Adhesive dental resins are widely used in dental clinics. They showed superior adhesiveness to tooth, metals and porcelains, etc. Most dental bonding agents contain carboxylic acid or phosphoric acid ester monomers for improving their adhesiveness to tooth substrate (1, 2).

The polymers with phosphate (P) groups are expected to bind calcium (Ca) ions under physiological conditions. It has been reported that the apatite is deposited on polyethylene and polyethyleneterephthalate films when they have been grafted with a P-containing polymer and soaked in a solution saturated with Ca and P ions (3–5). The polymer surface grafted with methacrylate phosphate monomer could induce hydroxyapatite (HA) deposition under a physiological condition to produce a thin HA layer onto the substrate. An organophosphate polymer becomes chemically bound onto a polymer film by surface graft polymerization of P-containing monomer, because the P group is one of the building blocks of HA and, in addition, should have a high affinity toward Ca ions. Mucaro *et al.* (6), Yokogawa *et al.* (7) and Varma *et al.* (8) reported that cotton, chitin fibres or chitosan film form calcium phosphate on their surface in solutions with ion concentrations 1·5 times those of simulated body fluid when they have been phosphorylated and subsequently soaked in saturated calcium hydroxide solution. The P groups of phosphoric ester monomers in dental bonding agents will be exposed on the surface after the curing of dental bonding agents.

On the basis of the above reports, it is expected that dental bonding agents containing phosphoric acid ester will induce a calcium phosphate layer on the cured bonding agents by the immersion in a simulated physiological solution. If dental polymers with P groups form a calcium phosphate layer on the materials *in vivo*, they could be useful as remineralization induction materials in dental clinics, for example, new types of direct pulp capping materials, or hyper-desensitizer reagents.

To our knowledge, there has been no previous reports on the calcium phosphate induction on the phosphorylated dental resins after the immersion in a electrolyte solution.

In the present study, we selected a commercially available dental bonding agent which contained phosphoric acid ester monomer as a phosphorylated polymer, and studied mineral induction behaviour using a mineralization inductive solution on this materials *in vitro* as a first series of immersion experiments. The composition and properties of deposited calcium phosphate on the dental bonding agent were investigated after immersion in electrolyte solution.

Materials and methods

As a phosphorylated dental bonding agent, Clearfil Photobond®* was used. Clearfil Photobond contains Bis-GMA, triethyleneglycol dimethacrylate, and methacryloxydecyl hydrogen phosphate (MDP) (9). The structure of MDP is shown in Fig. 1. Methacryloxydecyl hydrogen phosphate has a phosphonic acid moiety, P-OH, P=O and phosphate moiety, P-O-C. A tape with a hole measuring 80 mm in diameter and 1 mm thickness was placed on the Teflon mould. After mixing the universal and catalyst liquid of Clearfil Photobond, the mixture was applied inside the hole of the adhered tape. The bonding agent was cured by 60 s photo-irradiation using α-Light II† and heat-cured at 50 °C for 2 h, then at 100 °C for 30 min. The surface of cured bonding agent was polished using no. 1500-water proof paper under running water in order to remove the residual monomers on the surface of bonding agent. The cured Photobond disk was used as a phosphorylated polymer disk.

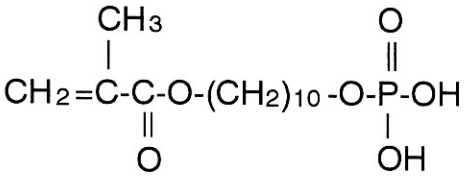

Fig. 1. Structure of methacryloxydecyl hydrogen phosphate (MDP).

Table 1. Ion concentrations in a Hank's balanced salt solution without organic species

Ion	Concentration (mmol L^{-1})
Na^+	142
K^+	5·81
Mg^{2+}	0·811
Ca^{2+}	1·26
Cl^-	145
HPo_4^{2-}	0·778
So_4^{2-}	0·811
HCo_3^-	4·17

The cured Photobond disks were then immersed in 30 mL electrolyte solution with pH = 7·4 at 37 °C for 1, 3, 5, 7, 14 and 28 days in sealed polystyrene bottles. The solution with pH 7·4 was Hanks' balanced salt solution (HBSS) without organic species, which was proposed by Hanawa (10) and Hanawa and Ota (11). The ion concentrations of HBSS are summarized in Table 1. The solutions and bottle were exchanged every day to expose the specimens to fresh solutions. Immediately after immersion, the specimens were again washed by deionized water to remove electrolytes that they did not take up. The specimens were then immediately dried in a desiccator.

The crystallographic structure of products of the immersion experiment at 7 days was analysed by means of thin-film X-ray diffraction‡ (XRD, thin-film attachment) utilizing CuKα-radiation, 50 kV, 250 mA. The surface of cured Photobond disk before immersion were also analysed by Fourier-transform infrared (FT-IR)§ spectrometer in reflection method. The immersion products at 7 days were removed from polymer disk, and their FT-IR spectrum was measured in KBr method. Preliminary experiments showed that it was very difficult to distinguish the peaks derived from

*Kuraray Co. Ltd, Osaka, Japan.
†J.Morita, Tokyo, Japan.
‡Rigaku, RINT 2000, Tokyo.
§Horiba, FT-210, Tokyo.

MDP and calcium phosphate when the immersed samples were measured by reflection method. Analyses were carried out at a constant resolution of 4 cm^{-1}.

The components and Ca and P contents of immersion products were analysed by electron probe microanalysis (EPMA)[¶] at an accelerating voltage of 25 kV. The specimens were coated by carbon before the EPMA measurement. The measured area was 50 × 50 μm. The intensities of Ca-Kα and P-Kα were measured at 1, 3, 5, 7, 14 and 28 days immersion. The Ca/P ratio was obtained from the calculated value of Ca and P with ZAF (Z: Atomic Number Effect, A: Absorption Effect, F: Flourescence Excitation Effect) quantitative correction. The morphology of the reaction products was observed by Field-emission scanning electron microscope (FE-SEM)** at an accelerating voltage of 5 kV. The specimens were coated with platinum before FE-SEM observation.

Results

The formation of white precipitates was observed on the phosphorylated polymer disk, i.e. cured Photobond disk, although no precipitation was observed in test solutions or on the wall of the bottle used for immersion during the experiments. The white precipitates on the cured phosphorylated polymer disk become visible after 3 days immersion in HBSS. After 7 days immersion, surface of the phosphorylated polymer disk was almost covered with white substance layers.

Figure 2 shows the XRD spectrum of white precipitates on the phosphorylated polymer disk after 7 days immersion. Major peaks in the spectrum could be assigned as 002, 210, 211, 112, 202, 310, 113, 222, 213 and 004 of peaks of hydroxyapatite as shown in Fig. 1. X-ray diffraction revealed that hydroxyapatite deposited on the phosphorylated polymer disk.

The FT-IR spectrum of exposed surface of phosphorylated polymer disk is shown in Fig. 3. The peaks between 1000 and 1300 cm^{-1} could be assigned as P=O and P-O-C stretching modes, and the peak around 2700 cm^{-1} could be assigned as P-OH stretching mode of organic phosphonic compounds. The broad peak around 3500 cm^{-1} was attributed as OH of P-OH.

Figure 4 shows the FT-IR spectrum of white precipitates on the phosphorylated polymer disk after 7 days

[¶]Hitachi, X-8010, Tokyo.
**JEOL, JSM-6340F, Tokyo.

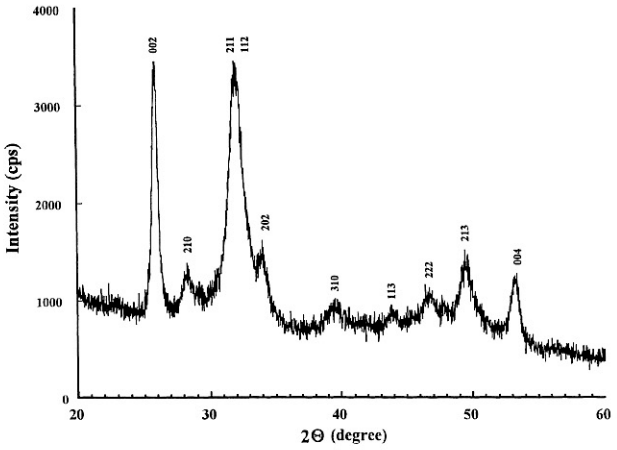

Fig. 2. X-ray diffraction (XRD) spectrum of white substance formed on a cured phosphorylated polymer disk after 7 days immersion in Hanks' balanced solution (HBSS).

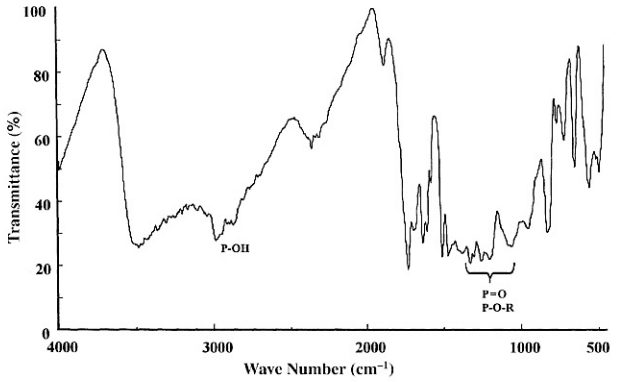

Fig. 3. Fourier-transform infrared (FT-IR) spectrum of the surface of cured phosphorylated polymer disk before immersion in Hanks' balanced solution (HBSS).

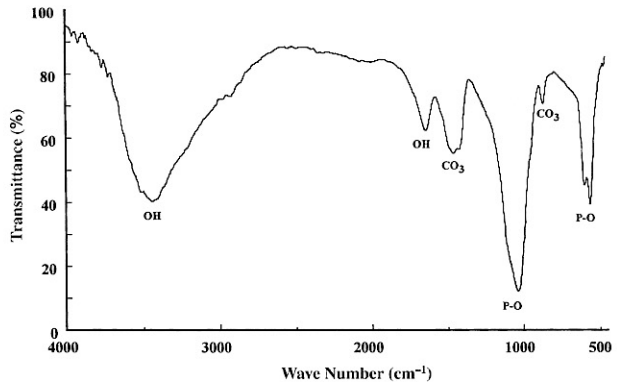

Fig. 4. Fourier-transform infrared (FT-IR) spectrum of white substances formed on a cured phosphorylated polymer disk after 7 days immersion in Hanks' balanced solution (HBSS).

	Immersion periods (day)					
	1	3	5	7	14	28
Calcium (Ca) (cps)	33 (4)	371 (115)	682 (13)	723 (19)	892 (101)	927 (41)
Phosphate (P) (cps)	57 (9)	195 (48)	316 (3)	342 (11)	379 (19)	372 (11)
Ca/P	0·37 (0·01)	1·41 (0·02)	1·43 (0·05)	1·37 (0·03)	1·90 (0·09)	1·82 (0·08)

Values expressed in parenthesis are standard deviation.

Table 2. Results of electron probe microanalysis (EPMA) analysis of the white substances after immersion in Hanks' balanced salt solution (HBSS)

immersion in HBSS. There are two clusters of peaks at 570 and 600 cm^{-1}, and at 1040 cm^{-1}. The former cluster was assigned as P-O bending modes, and the latter was assigned as P-O stretching mode. These are attributed to the P-O bonds of inorganic calcium phosphate materials. The peaks around 1635 and 3450 cm^{-1} were assigned as hydroxyl group of a hydroxyapatite. The peaks derived from carbonate groups were also observed around 870 and 1420 cm^{-1}, indicating that this carbonate groups were incorporated in the apatite structure.

The component of white precipitates was analysed by EPMA. Electron probe microanalysis revealed that the components of white precipitates were Ca, P and O. The intensities of Ca and P and Ca/P ratio of white precipitates were listed in Table 2. The amounts of Ca and P were increased according to the length of immersion periods. After 3 days immersion, the amounts of Ca and P remarkably increased as shown in Table 2. The slight increase of the amounts of Ca and P was observed after 5, 7, 14 and 28 days immersion.

The Ca/P ratio of white substance was about 1·4 at 3, 5, 7 days immersion periods. After 14 and 28 days immersion, the Ca/P ratio was raised to 1·90 and 1·82, respectively.

Figure 5 showed FE-SEM pictures of the surface of the phosphorylated polymer disk after the immersion in HBSS. Scanning electron microscopic observation revealed that there was no precipitate formation on the Photobond polymer surface after 1 day immersion. After 3 days immersion, the formation of precipitated globules was observed. The globules were scattered on the polymer surface. The number of globules was increased at 5 days immersion, but the polymer surface was not completely covered with the globules. After 7 days immersion, the polymer surface was completely covered with calcium phosphate globules. A large number of globules was fused together, and smaller globules were present on the top of fused globules. After 14 and 28 days, new globules were piled up on the precipitated globules. There were no distinct differences in the appearances between 14 and 28 days immersion.

Higher magnification FE-SEM observation of white precipitates (Fig. 6) revealed that each globule was composed of a group of numerous thin-film form flakes uniting and/or clustering together on the phosphorylated polymer disk. The size of flakes was between 100 and 200 nm after both 7 and 28 days immersion. This type of crystal agglomeration was referred as card-house structure.

Discussion

This study revealed that carbonate-containing hydroxyapatite was formed on the phosphorylated polymer disk, i.e. cured Photobond disk, after the immersion of HBSS.

The phosphoric ester monomer, MDP, was incorporated in phosphorylated polymer (9). Fourier-transform infrared spectrum revealed that P-OH group of MDP was existed on the exposed polymer surface after curing. It is presumed that P-OH of MDP dissociates into $P\text{-}O^-$ and H^+ in HBSS and that some dissociated phosphate groups, $P\text{-}O^-$, interact with Ca ions of HBSS. It is also possible that Ca ions interact with partly negative charged oxygen P=O and P-O-C of MDP. Subsequently, Ca ions were adsorbed onto the phosphorylated polymer disk. Afterwards, P ions of HBSS interact with pre-adsorbed Ca ions and then are adsorbed on the Ca pre-adsorbed surface. The P-OH group, P=O and P-O-C of MDP served as a template of a spatial cage for nucleation and growth of calcium phosphate. The calcium phosphate layer is probably formed by repetition of this process.

The carbonate ions were incorporated into the hydroxyapatite and thus carbonate-containing hydroxyapatite formed on the phosphorylated polymer because of the rich amount of carbonate ions in HBSS. Hanawa (10) and Hanawa and Ohta (11)

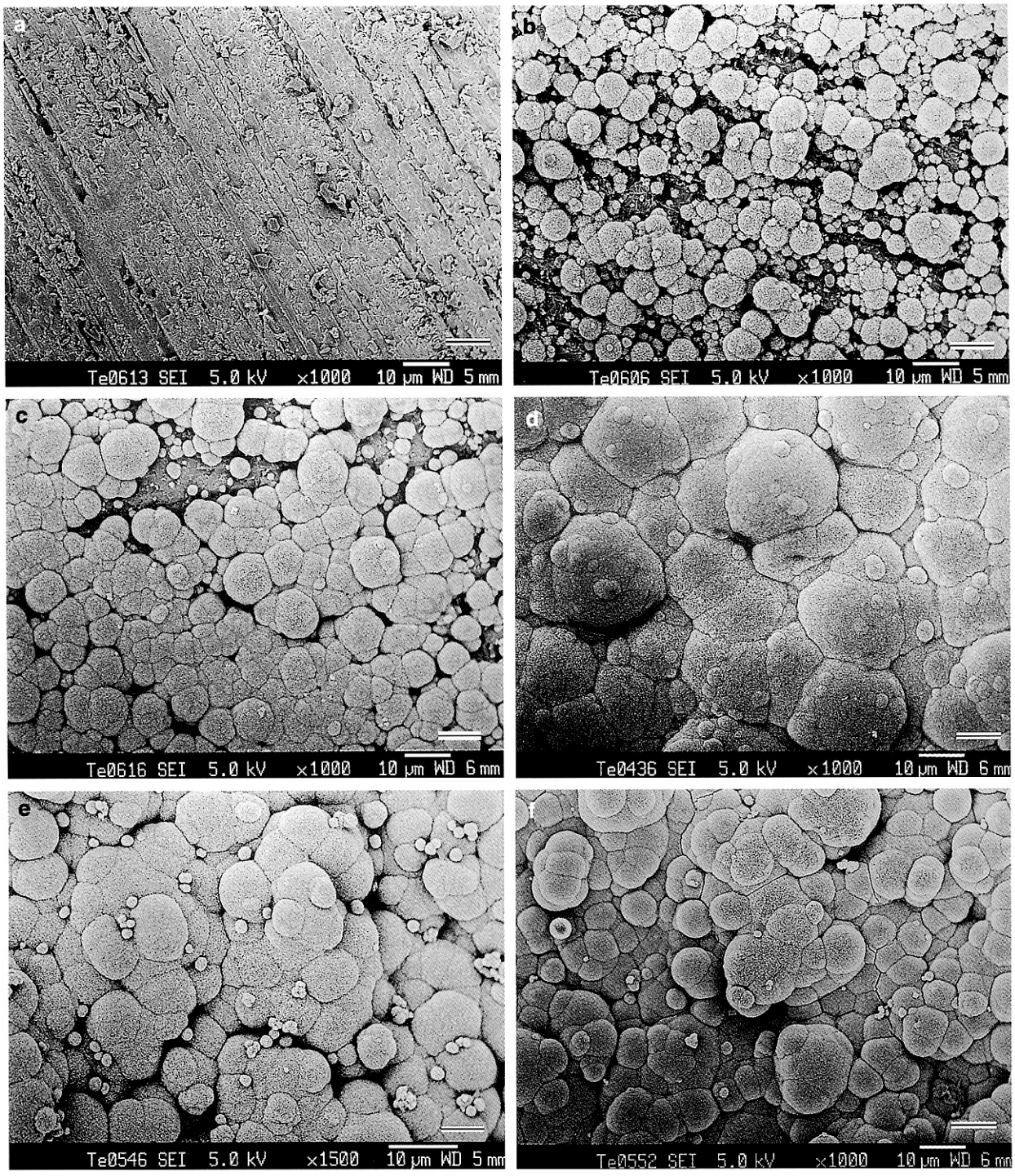

Fig. 5. Field-emission scanning electron microscope (FE-SEM) pictures of the surface of phosphorylated polymer disk after the immersion in Hanks' balanced salt solution (HBSS). (a) 1 day immersion in HBSS. Polished surface of the polymer was observed. There was no precipitation (bar = 10 μm). (b) 3 days immersion in HBSS. The formation of precipitated globules was observed. The globules are scattered on the phosphorylated polymer surface (bar = 10 μm). (c) 5 days immersion in HBSS. The number of globules were increased, but the phosphorylated polymer surface was not completely covered with calcium phosphate globules (bar = 10 μm). (d) 7 days immersion in HBSS. The phosphorylated polymer surface was completely covered with calcium phosphate globules (bar = 10 μm). (e) 14 days immersion in HBSS. The new globules were plied up on the precipitated globules (bar = 10 μm). (f) 28 days in immersion in HBSS. The appearances were almost same as those of 14 days immersion sample (bar = 10 μm).

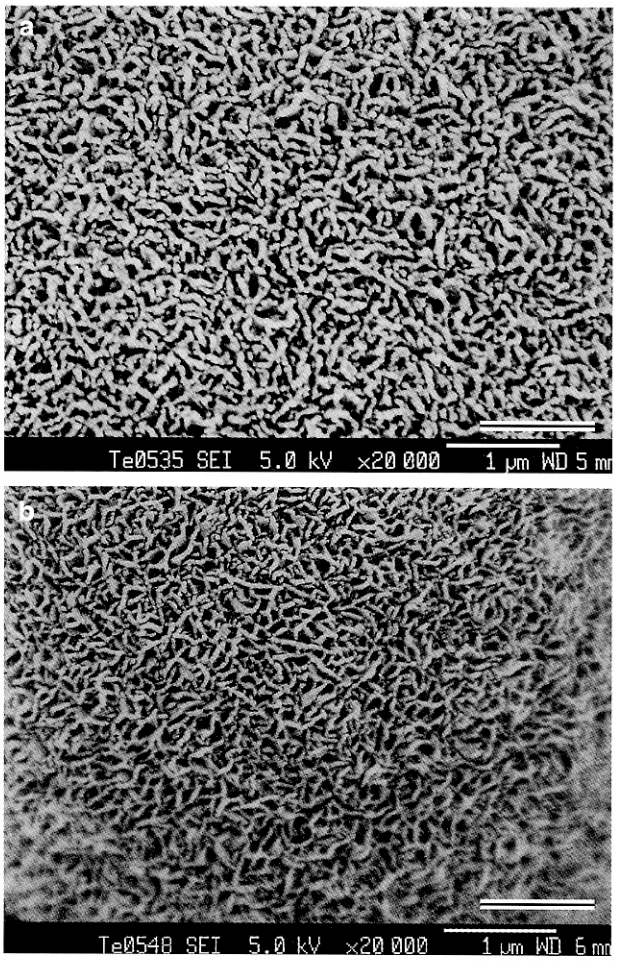

Fig. 6. Higher magnification field-emission scanning electron microscope (FE-SEM) pictures of white precipitates on the phosphorylated polymer disk after the immersion in Hanks' balanced solution (HBSS) at 7 days (a) and at 28 days (b). Each globule was composed of numerous thin-film form flakes uniting and/or clustering together. The size of flakes was between 100 and 200 nm (bar = 1 μm).

found that calcium phosphate deposited on titanium after the immersion in HBSS, and reported that the calcium phosphate was carbonate-containing hydroxyapatite. Their results corresponded with our results. However, they reported that carbonate-containing hydroxyapatite was obtained on titanium surface after 60 days immersion. Serro *et al.* (12) also reported there was no calcium phosphate precipitation on titanium after 7 days of immersion in HBSS. In this study, we observed hydroxyapatite formation on cured Photobond disk after 3 days HBSS immersion macro- and microscopically. This was due to the difference of the surface chemistry of titanium and phosphorylated polymer, namely with or without of phosphonic acid and P group. The present study revealed that the presence of phosphonic acid and P group was favourable for the precipitation of hydroxyapatite.

The Ca/P ratio of deposited hydroxyapatite did not correspond with the theoretical value of hydroxyapatite. The Ca/P ration was less than 1.67 until 7 days immersion, and that was greater than 1.67 after 14 days immersion. Electron probe microanalysis was performed at 25 kV and the depth of detection at this condition was predicted about 2.5 μm. The reduced Ca/P ratio was due to the detection of the phosphorus of phosphorylated polymer disk besides the phosphorous of deposited apatite. The reason for the greater Ca/P ratio after 14 days immersion was not clear. The deposition of calcium phosphate besides hydroxyapatite, for example, tetracalcium phosphate, was a possibility. The detailed mechanism for the deposition of calcium phosphate should be further investigated.

It is widely known that a phosphorylated bonding agent such as Photobond shows good adhesiveness to tooth substrate (13–15). Phosphorylated bonding agent is also used as a direct pulp capping material, and it is reported that there were no severe pulpal reactions after direct pulp capping with a phosphorylated bonding agent (16–19).

In the present study, we found a new function of Photobond which is a phosphorylated bonding agent. Phosphorylated bonding agent can induce the formation of calcium phosphate on its surface after the immersion of HBSS. The main component of induced calcium phosphate was carbonate-containing hydroxyapatite. The results obtained in this study suggested that other phosphorylated bonding agents besides Photobond have a possibility to induce calcium phosphate formation *in vitro*. Tsuneda *et al.* (20) observed the formation of secondary dentin on the exposed pulp of rat after the direct pulp capping with phosphorylated bonding agent. It is presumed that the remineralization induction ability of phosphorylated bonding agent such as Photobond participate in secondary dentin formation when used as direct pulp capping material. The formation of calcium phosphate *in vitro* should be further investigated.

Acknowledgments

This study was supported in part by a grant from the Ministry of Education, Culture, Sports, Science and

Technology to multidisciplinary research projects and to promote 2001-Multidisciplinary Research Projects (in 2001–2005), grants-in-aid for Research for the Frontier Science from the Ministry of Education, Culture, Sports, Science and Technology of Japan, and grants-in-aid for Scientific Research (C)(2)(nos 11671817, 12671904) from Japan Society for the Promotion of Science. This study was also supported in part by Oral Health Science Center grant 992C01 from Tokyo Dental College.

References

1. Erickson RL. Surface interactions of dentin adhesive materials. Oper Dent. 1992;Suppl. 5:81.
2. Perdigao J, Lopes M. Dentin bonding – state of the art 1999. Compend Contin Educ Dent. 1999;20:1151.
3. Tretinnikov ON, Kato K, Ikada Y. *In vitro* hydroxyapatite deposition onto a film surface-grafted with organophosphate polymer. J Biomed Mater Res. 1994;28:1365.
4. Kato K, Eika Y, Ikada Y. Deposition of a hydroxyapatite thin layer onto a polymer surface carrying grafted phosphate polymer chains. J Biomed Mater Res. 1996;32:687.
5. Kamei S, Naohide T, Tamai S, Kato K, Ikada Y. Histological and mechanical evaluation for bone bonding of polymer surfaces grafted with a phosphate-containing polymer. J Biomed Mater Res. 1997;37:384.
6. Mucaro MR, Yokogawa Y, Toriyama M, Suzuki T, Kawmoto Y, Nagata F et al. Growth of calcium phosphate on surface-modified cotton. J Mater Sci Mater Med. 1995;6: 597.
7. Yokogawa Y, Reyes JP, Mucalo MR, Toriyama M, Kawamoto Y, Suzuki T et al. Growth of calcium phosphate on phosphorylated chitin fibres. J Mater Sci Mater Med. 1997;8:407.
8. Varma HK, Yokogawa Y, Espinosa FF, Kawamoto Y, Nishizawa K, Nagata F et al. Porous calcium phosphate coating over phosphorylated chitosan film by a biomimetic method. Biomater. 1999;20:879.
9. Fujisawa S, Kadoma Y, Komoda Y. HPLC separation of methacryloyloxydecyl dihydrogen phosphate from dental bonding agent. J Jpn Soc Dent Mater Devices. 1991;10:30.
10. Hanawa T. Titanium and its oxide film: a substrate for formation of apatite. In: Davies JE, ed. The Bone–Biomaterial Interface. Toronto: University Tronto Press, 1991: 49.
11. Hanawa T, Ota M. Calcium phosphate naturally formed on titanium in electrolyte solution. Biomater. 1991;12:767.
12. Serro AP, Fernandes AC, Saramago B, Lima J, Barbosa MA. Apatite deposition on titanium surfaces – the role of albumin adsorption. Biomater. 1997;18:963.
13. Hirasawa K, Fujitani M, Hosoda H. Studies of newly designed tooth surface treatments for adhesive composite restoration. Bull Tokyo Med Dent Univ. 1992;39:19.
14. Fortin D, Swift EJ Jr, Denehy GE, Reinhardt JW. Bond strength and microleakage of current dentin adhesives. Dent Mater. 1994;10:253.
15. Tyas MJ. Clinical evaluation of five adhesive systems. Am J Dent. 1994;7:77.
16. Kashiwada T, Takagi M. New restoration and direct pulp capping systems using adhesive composite resin. Bull Tokyo Med Dent Univ. 1991;38:45.
17. Onoe N. Study on adhesive bonding systems as a direct pulp capping agent. Jpn J Conserv Dent. 1994;37:429.
18. Kato Y, Kimura T, Inaba T. Clinicopathological study on pulp-irritation of adhesive resinous materials. Jpn J Conserv Dent. 1997;40:153.
19. Akimoto N, Monoi Y, Kohno K, Suzuki S, Otsuki M, Suzuki S et al. Biocompatibility of Clearfil Liner Bond 2 and Clearfi AP-X system on nonexposed and exposed primate teeth. Quintessence Inter. 1998;29:177.
20. Tsuneda Y, Hayakawa T, Yamamoto H, Ikemi T, Nemoto K. A histopathological study of direct pulp capping with adhesive resins. Oper Dent. 1995;20:223.

Correspondence: Dr Tohru Hayakawa, Department of Dental Materials, Nihon University School of Dentistry at Matsudo, 2-870-1, Sakaecho-nishi, Matsudo, Chiba 271-8587, Japan.
E-mail: hayakawa@mascat.nihon-u.ac.jp

Int J Oral-Med Sci 2(1):50-53, 2004

Case Report

An Unusually Large Submandibular Salivary Calculus: Case Report and Structural Analysis

Yoshiaki Akimoto,[1] Toshiro Sakae,[2] Chie Toyoda,[1] Makiko Ono,[1] Kazuhiro Hasegawa,[1] Shigeo Tanaka,[1] Jun Shibutani,[1] Takashi Kaneda,[3] Takeshi Maeda,[4] Teruyasu Hirayama,[4] Akira Fujii,[5] Hirotsugu Yamamoto,[6] and Racquel Z LeGeros[7]

Departments of [1]Oral Surgery, [2]Anatomy, [3]Radiology, [4]Neurological Surgery, [5]Pharmacology, and [6]Pathology, Nihon University School of Dentistry at Matsudo, Matsudo, Chiba 271-8587, Japan
[7]Department of Biomaterials and Biomimetics, New York University College of Dentistry, New York, NY, USA

Correspondence to: Yoshiaki Akimoto
E-mail: yoshi@mascat.nihon-u.ac.jp

Key words:
large calculus, submandibular duct, structural properties, X-ray diffraction

Abstract

We present a case involving an unusually large calculus of Wharton's duct. To gain insight into the formation of this calculus, detailed structural properties were investigated using an X-ray diffraction technique. A 70-year old man, brought a calculus to a dental consultation, by himself, when it perforated the floor of the mouth. The calculus was unusually long, measuring 4.5 cm in length. X-ray diffraction and micro-FT-IR analyses were employed to investigate structural properties of the calculus, which suggested that its stratified structure, reflecting compositional changes in the microenvironment, was a result of intermittent and incremental growth.

Introduction

Sialolithiasis accounts for more than 50% of diseases of the major salivary glands and is thus the most common cause of acute and chronic infections at these sites. More than 80% of calculi occur in the submandibular gland or its duct, 6% in the parotid gland and 2% in the sublingual gland or minor salivary glands (1). Sialolithiasis in the submandibular gland or its duct can cause symptoms, consisting of pain or discomfort before or during meals, or can be asymptomatic. Associated recurrent submandibular swelling is often described. Clinically, calculi are round or ovoid, rough or smooth, and are of a yellowish color, varying in size from a few millimeters up to several centimeters, although such large calculi are rare (2,3). The calculus described in the present report is of interest owing to its size and shape, particularly as it was removed by the patient himself. In order to gain insight into the formation of this sialolith, detailed structural properties were determined using X-ray diffraction analysis and micro fourier transform infrared analysis (Micro FT-IR).

Case Report

A 70-year-old man visited a dental practitioner requesting new dentures, and gave a history of intermittent swelling and pain in the right submandibular region during meals for the previous 5 years. Oral examination showed a swelling of the right sublingual region. Bimanual palpation of the oral floor indicated the swelling to be a mass that was hard, smooth and painless, and measured approximately 3 cm in length. The overlying mucosa was normal in color. Panoramic radiography revealed a single, well-defined, homogenous radiopaque mass in the floor of the mouth, extending from the mandibular canine area to the mandibular angle (Fig. 1). A diagnosis of submandibular sialolithiasis was made and the dentist recommended examination by an oral surgeon. However, three weeks after the dental consultation, before the patient had attended the referral appointment, the tip of calculus perforated through the floor of the mouth. The patient removed the calculus by himself and brought it to the dentist and to our hospital. The calculus was long and tapered in shape, yellowish white in color, 4.5 x 0.7 cm in length and width, and 1.34 g in dry weight (Fig.

Fig. 1. Panoramic radiograph showing a long radiopacity superimposed over the right mandibular cuspid area and the mandibular angle region.

2). Panoramic radiography at this point revealed that the calculus had been removed in its entirety (Fig. 3). Compared to that of the other side, the affected submandibular gland was noted to smaller and harder after calculus removal because of atrophy and fibrosis; however, salivary secretion was unimpeded and the patient had no complaints. Subsequent follow-up over three years was uneventful.

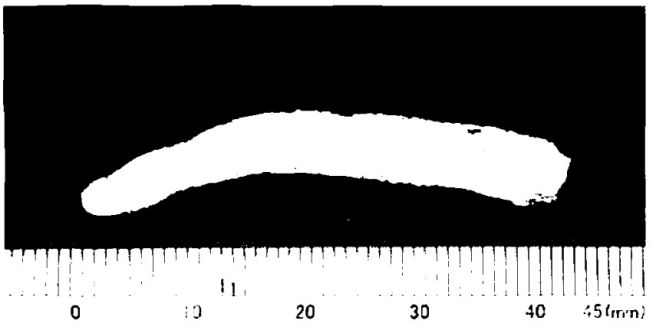

Fig. 2. A 4.5-cm long calculus shown to scale. The right side of the calculus was exposed within the oral floor.

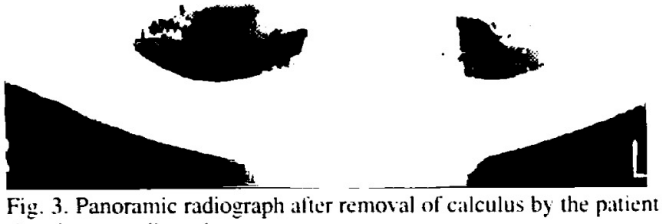

Fig. 3. Panoramic radiograph after removal of calculus by the patient showing no radiopacity.

Analysis of the Calculus

In order to gain insight into the formation of this calculus, its detailed structural properties were investigated. Three X-ray diffraction (XRD) analytical techniques were employed to reveal the crystallographic characteristics of the calculus: conventional XRD for bulk analysis, micro-XRD for point analysis and crystal orientation analysis, and selected-area XRD (SA-XRD) for analysis of specific selected regions. This combination of modalities, has the potential to achieve the data accuracy of conventional XRD and a spatial resolution for point-analysis similar to that of micro XRD(4). Micro fourier transform infrared analysis (Micro FT-IR) was also used to reveal carbonate and phosphate composition.

Conventional XRD patterns demonstrated the structure and diffraction peak broadening usually observed in biologic apatite (Fig. 4). No other crystalline phase was detected in this analysis.

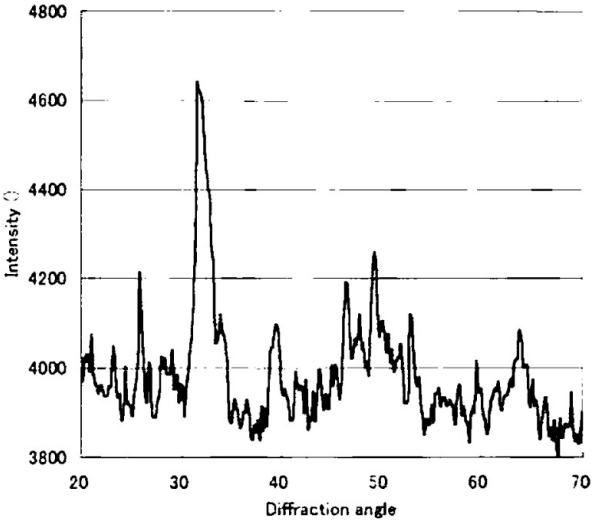

Fig. 4. Conventional XRD pattern showing a diffraction pattern consistent with apatite.

A series of micro-XRD images of the calculus revealed slight differences in the preferred crystal orientation among neighboring points and conversion of this micro-XRD data to determine powder pattern identified the crystals as apatite (Fig. 5a, b).

All 60 SA-XRD patterns of the calculus were consistent with apatite (Fig. 6); however, small differences in peak

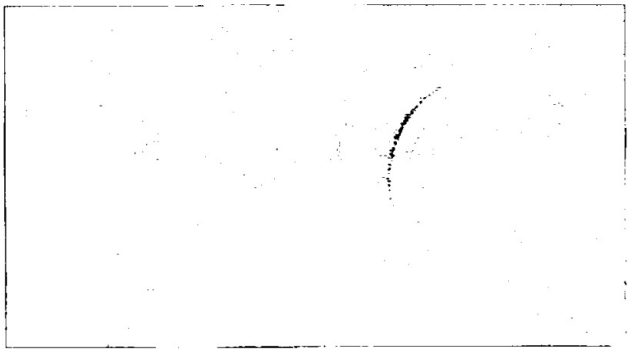

micro-diffractogram recorded on an imaging plate.

positions were noted within the analyzed area, indicating possible differences in composition of the apatite.

Micro-FT-IR analysis revealed the main constituent of the calculus to be carbonate hydroxyapatite, with carbonate absorption bands appearing at around 1,400 cm^{-1} and 1,600 cm^{-1} (Fig. 7).

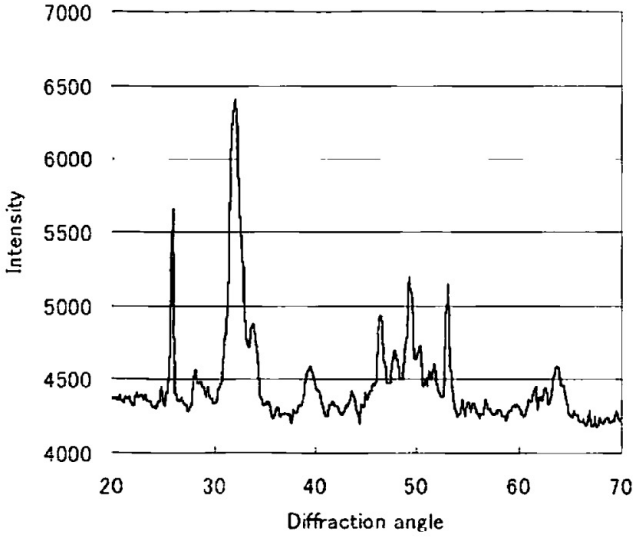

Fig. 5b. The diffraction pattern converted from Figure 5a.

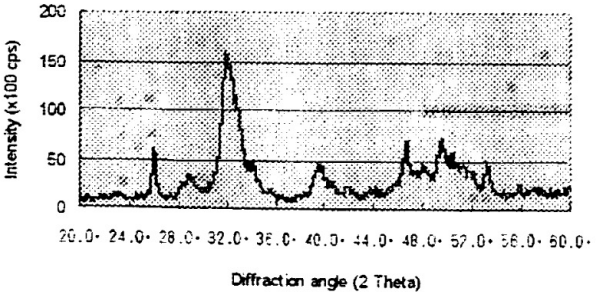

Fig. 6. SA-XRD pattern of the calculus showing apatite diffraction peaks.

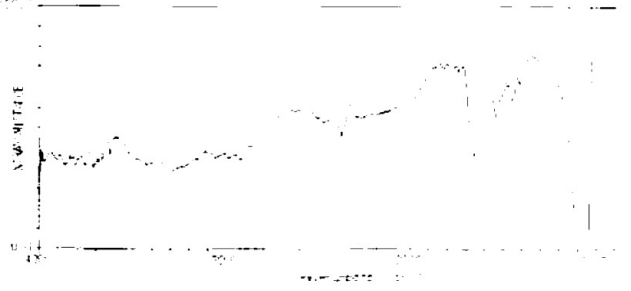

Fig. 7. Micro FT-IR spectrum of the sialolith showing the absorption bands of phosphate ions at about 1050 cm^{-1} and the bands of carbonate ions at about 1450 cm^{-1} and 1550 cm^{-1}.

Table 1. Review of literature reports of calculus measuring 4 cm or more in the submandibular gland or duct

Author	Age	Sex	Size (cm)	Weight (g)[1]
Martin (5)	60	M	6 x 1.5	-
Mustard(6)	42	M	5.6	-
Raksin (7)	52	M	5.5 x 2	9.5
Hubar (8)	65	M	5.2	17.5
Eiraku[2]	56	M	5.1 x 1.1	3.5
Koshal (9)	40	M	5.0 x 2.8	-
Meyers (10)	50	M	5 x 3.0	2.8
Tinsley (11)	48	M	5	23.56
Present case	70	M	4.5 x 0.7	1.34

[1] Dry or wet weight.

[2] Abstract of 53rd Annual Meeting of Japanese Stomatological Society, Eiraku D et al.: A case of large intraductal sialolith, No. 1-F-53, 1999.

Discussion

Reports of large calculi (measuring 4 cm or more in length) within the submandibular gland or its duct are summarized in Table 1. In all cases, patients were males aged over 40 (5-11). Martin *et al.* (5) reported the largest calculus (length, 6 cm), with the present case (4.5 cm) ranking 9th in size. Calculus shape was cylindrical except in the cases reported by Koshal *et al.* and Tinsley, in which oval calculi were identified (6,11). The present case represents the only report in which the calculus was not surgically extracted. Since the calculus was long and extremely narrow in shape and its tip happened to perforate the anterior part of the floor of the mouth, the patient could easily pull it out. Although a perforation of the floor of the mouth is more likely occur in cases of anterior ductal calculus than in those involving the posterior duct (12-14), it is very rare for patients to remove calculi by themselves.

Three types of XRD were employed to reveal the crystallographic characteristics of the calculus. Conventional XRD, showed the sialolith to be composed of apatite, micro-XRD demonstrated the preferred crystal orientation, and SA-XRD revealed inhomogeneity in the chemical composition from layer to layer. Intermittent growth of the apatite crystals was confirmed by crystal orientation analysis.

X-ray diffraction analysis provided information on the crystal-line phases present in the sialolith (15,16). However, diffraction peaks of the apatite crystals in the calculus were

too broad to allow accurate analysis. Variations in unit cell dimensions strongly suggested changes in apatite composition, reflecting alterations in micro environmental conditions and composition of the calculus (16).

Detailed investigations of crystalline structure are not generally performed when patients with sialolithiasis; however, we believe that analysis of crystalline phase, composition, and orientation could lead to a better understanding of the formation mechanism of calculus.

References

1. Zenk J, Benzel W, Iro H: New modalities in the management of human Sialolithiasis. Minimal Invasive Therap, 3:275-284, 1994.
2. Waal I, Kwast WAM. Oral Pathology. In: Salivary gland diseases, Sialolithiasis, 1st ed, 1988, Quintessence Pub, Chicago, USA p. 254-255.
3. Fuchihata H. Oral and Maxillofacial Radiology Today. In: Akimoto Y, Sakae T, Kaneda T et al., A long submandibular sialolith lying in the Wharton's duct, Elservier, Amsterdam, Netherlands, 2000. p. 615-617.
4. Sakae T, Akimoto Y, Kaneda T et al.: Intermittent crystal growth of unusually long submandibular sialolith revealed by micro-focus- and selected-area- X-ray Diffraction. J Hard Tissue Biol, 12:25-28, 2003.
5. Martin PA, Alonso T JL, Wscapa GJ, Capa F: Giant calculus of the submaxillary gland. Acta Otorrinolaringo Esp, 41:265-267, 1990.
6. Mustard TA: Calculus of unusual size in Wharton's duct.. Br Dent J, 79:129, 1945.
7. Raksin SZ, Could ST, Williams AC: Submandibular duct sialolith of unusual size and shape. J Oral Surg, 33:142-145, 1975.
8. Hubar JS, Guggenheimer J, Evan M: Megalith. Oral Surg Oral Med Oral Pathol, 70: 245,1990.
9. Koshal KD, Naik RS: Giant submaxillary sialolith. J Ind Med Assoc, 77:14-15, 1981.
10. Meyers H: Large salivary calculus in submaxillary gland. Dent Dig, 48:420-421, 1942.
11. Tinsley G: An extraordinarily large asymptomatic submandibular salivary calculus. Br Dent J, 166:199, 1989.
12. El Deeb M, Holte N, Gorlin RJ: Submandibular salivary gland sialoliths perforated through the oral floor. Oral Surg, 51:134-139, 1981.
13. Paul D, Chauhan SR: Salivary megalith with a sialo-cutaneous and sialo-oral fistula: a case report. J Laryngol Otol, 109:767-769, 1995.
14. Sutay S, Erdag TK, Ikiz AO, Guneri EA: Large submandibular gland calculus with perforation of the floor of the mouth: Otolaryngol Head Neck Surg, 128:587-588, 2003.
15. Boskey AL, Burstein LS, Mandel ID: Phospholipids associated with human parotid gland sialoliths. Arch Oral Biol, 28:655-657, 1983.
16. LeGeros RZ: Oral Biology and Medicine, Calcium phosphates, 1991. Karger, Basel, Switzerland

Journal of Hard Tissue Biology 12[1] (2003) p25-28

CODEN-JHTBFF, ISSN 1341-7649

ORIGINAL

Intermittent Crystal Growth of Unusually Long Submandibular Sialolith Revealed by Micro-Focus- and Selected-Area- X-Ray Diffraction.

Toshiro SAKAE[1], Yoshiaki AKIMOTO[2], Takashi KANEDA[3], Akira FUJII[4], Tadahiko UTSUNOMIYA[5], Hirotsugu YAMAMOTO[5], Takaatsu HARADA[2], Kazuo HIGUCHI[2], Seiichi. SATO[2] and Racquel.Z. LeGeros[6]

[1]*Department of Oral Histology, Nihon University School of Dentistry at Matsudo, Chiba, 271-8587, Japan,*
[2]*Department of Oral Surgery, Nihon University School of Dentistry at Matsudo, Chiba, 271-8587, Japan,*
[3]*Department of Radiology, Nihon University School of Dentistry at Matsudo, Chiba, 271-8587, Japan,*
[4]*Department of Pharmacology, Nihon University School of Dentistry at Matsudo, Chiba, 271-8587, Japan,*
[5]*Department of Oral Pathology, Nihon University School of Dentistry at Matsudo, Chiba, 271-8587, Japan,*
[6]*Department of Biomaterials and Biomimetics, New York University College of Dentistry, New York, New York, USA*
(Accepted for publication : May 30, 2003)

Abstract: BACKGROUND: Sialolith is a pathological calcification found inside salivary glands, composed principally of apatite crystals. The purpose of this study was to investigate detailed structural properties to gain insight into the formation of sialolith. METHODS: A 45 mm long sialolith from a human submandibular gland was studied using micro-FTIR and three types of X-ray diffraction (XRD) techniques: i) conventional, ii) micro-focus, and iii) "selected-area XRD" (SA-XRD). RESULTS: The longitudinal section of the sialolith showed a stratified structure perpendicular to the long axis. XRD and FTIR showed that the bulk of the sialolith was composed of carbonate hydroxyapatite. Micro-XRD revealed that crystal orientation was slightly different in each incremental zone. "SA-XRD" showed that the average unit cell dimensions of apatite crystals were different for each zone. CONCLUSION: These results suggest that the stratified structure in the sialolith was a result of intermittent and incremental additional growth reflecting compositional changes in the microenvironment.

Key words: Salivary Gland Calculi, Carbonate apatite, FTIR, X-Ray Diffraction

Introduction

Sialoliths are pathological calcifications sometimes occurring in the salivary glands. In our previous paper, we reported a 45 mm long sialolith from a submandibular Wharton's duct showing a stratified (banded) structure[1] similar to those observed in sialolith from other salivary glands[2,3]. In general, banded textures in hard tissues indicate that the calcification process occurred by intermittent growth. The banded structure observed in some sialoliths suggest intermittent mineralization [4]. Sialoliths consist of mostly a mineral phase. Like human dental calculus, the mineral phase of sialoliths is usually composed of different calcium phosphates (apatite, whitlockite, octacalcium phosphate), with apatite showing the greatest abundance and occurring in greatest frequency [5, 6, 7]. There is a clinical need for treatment and prevention of sialolithiasis. The purpose of this study is to investigate detailed structural properties of sialolith to gain insight into its formation. For this study, three X-ray diffraction (XRD) analytical techniques, in addition to FTIR, were used to reveal the crystallographic characteristics of the unusually long sialolith: conventional XRD for bulk analysis, micro XRD for point analysis and crystal orientation analysis, and a new technique, "selected-area XRD" for analysis of specific selected areas, having the potential of the data accuracy same to conventional XRD and the spatial resolution of point-analysis similar to that of micro XRD.

Correspondence to Toshiro. Sakae : Nihon University School of Dentistry at Matsudo, Chiba, 271-8587, Japan.Phone: 047-360-9323, FAX 047-360-9324, e-mail:sakae@mascat.nihon-u.ac.jp

Materials and methods

Salivary calculus used in this study was the unusually long sialolith from the submandibular Wharton's duct described in[1]. It is yellowish-white in color, a slightly bent and wedge-shaped cylindrical form with rounded end, 45 mm x 7 mm in size and 1.34 g in weight. The sialolith was cut longitudinally into halves for X-ray diffraction analysis. The sectioned plane showed a stratified texture normal to the long axis under a binocular scope. The histological and microscopic examination indicated that this sialolith was composed of intermittent layers of calcified materials. To investigate the crystallographic character of the sialolith, three kinds of X-ray diffraction analysis were carried out using the following conditions.

Conventional X-ray Diffraction (XRD)

For this powder-type of XRD analysis, data was collected using a RIGAKU RINT 2000, powder-type X-ray diffractometer, RIGAKU Co. Ltd. Tokyo, under the following conditions; X-ray generation: Cu rotary target, accelerating voltage: 50 kV, accelerating current: 200 mA, monochrometer: graphite plate crystal, X-ray wavelength: 1.5418 Angstrom (CuKα), detector: scintillation counter, scan speed: 1 degree (2θ/min), scan range: 3-120 degree (2θ). X-ray data analysis was carried out using JADE (Material Data Inc.), using conventional slit-system. The X-ray radiation area on the sample was 10mm x 20mm at the low angle region.

Micro X-ray Diffraction (Micro-XRD)

Micro-focus X-ray diffraction (micro-XRD) data of the sialolith from a point 100 μm in diameter was collected using a RIGAKU RINT RAPID with IP (imaging plate) system, RIGAKU Co. Ltd. Tokyo. The image data was digitally recorded and directly transferred to a computer. The experimental conditions were as follows; X-ray tube target: Cu, tube voltage: 50 kV, tube current: 30 mA, monochrometer: graphite plate crystal, X-ray wavelength: 1.5418 Angstrom (CuKα), collimator: 100 μm in diameter, Imaging Plate®(IP, Fuji Film Co. Ltd., Tokyo) recording system with IP size: 466 mm x 256 mm, camera radius: 127.4mm, pixel size: 100 μm x 100 μm, sample setting: reflection-mode, exposure time: 20 min. X-ray diffraction IP imaging analysis system: RIGAKU R-AXIS display software.

Selected-Area X-ray Diffraction (SA-XRD)

In this study, another type of micro-XRD analysis was applied. The auto-slit-width-arrange-system, equipped on the RIGAKU RINT 2000, allows a fixed X-ray exposed area on a sample plane at any given scanning angle by controlling the X-ray incident beam width. In this study, the X-ray exposed width was fixed at 1 mm on the sample plane, and then the radiation window area was 1mm width x 10mm length. The other experimental conditions were similar to the conventional XRD measurement. This method that we refer to as "Selected-Area X-ray diffraction" (SA-XRD), has not been used in the investigation of pathological materials. This method has some advantages in data-collection time, accuracy of data and data compatibility with conventional powder XRD method compared with the micro-focus XRD. Applying this method to the specimen, the window area of 1 mm in width was set perpendicular to the longitudinal axis of the sialolith. The unit cell dimensions were calculated using the JADE program.

Micro Fourier Transform Infrared Analysis (Micro FT-IR)

Carbonate and phosphate composition was analyzed using a micro FT-IR, HORIBA FT-530, under the following conditions; measurement mode: reflection, analyzing area: 20x100 μm, detector: MCT (cooling by LN_2), Cassegrain mirror: x4, measurement cycle: 60, resolution: $4cm^{-1}$, measurement range: 750-4000 cm^{-1}. The measurements were carried out at the positions where the XRD studies were carried out. The observed raw data was transformed to a pseudo-transmitting absorption spectrum by the Kramers-Krönig analysis.

Results

The long sialolith was divided into three portions namely as the thin head-portion, the body-portion at the middle and the thick tail-portion, for placing the sample in the sample holder (Fig. 1). The sialolith showed a stratified texture on the sectioned plane with a loose concentric pattern. These bands consisted of alternating narrow and wide bands. The wide bands were relatively glossy and transparent, suggesting that relatively large crystals are arranged in an organized manner in contrast with the crystals located in the narrow slightly brownish bands.

The conventional-type XRD patterns of the three portions showed apatite structure (Fig. 2). The conventional XRD patterns showed the diffraction peak broadening which was usually observed in biologic apatites. No other crystalline phase was detected in these patterns.

Micro-XRD IP images of thirty points on the sections of the three portions were obtained. An example of a micro-XRD pattern is shown in Fig. 3. The two-dimensional micro-XRD image clearly showed preferred crystal orientation as the strong 002 circular arc. A series of micro-XRD images of the sialolith showed that there were slight differences in the preferred crystal orientation among the neighboring points. The converted powder pattern of this micro-XRD data (Fig. 4) identified the crystals as apatite.

All the sixty SA-XRD patterns of the sialolith were identified as apatite (Fig. 5). There were small differences in the peak positions among the analyzed areas, indicating possible differences in composition of the apatite. The unit cell dimensions of the apatite crystals are summarized in Table 1. These values were slightly, but significantly, different from each other. The variations in the unit cell dimensions indicated that the crystals in incremental bands slightly differed in chemical composition resulting from changes in the type and amount of substituting ions in the apatite crystal

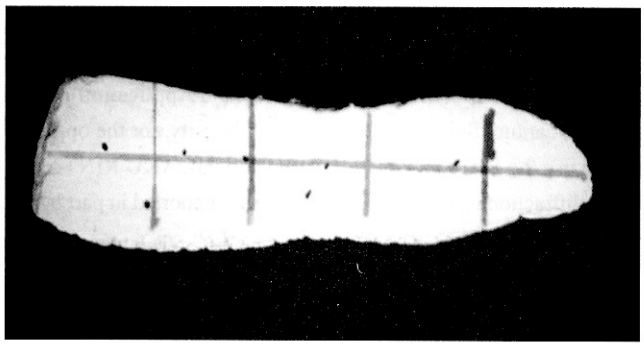

Fig. 1. Photograph of the head-portion section plane of the unusually long sialolith, showing the selected area analysis points at the cross-points of the lines. The tangential axis line also indicated the line of points for the micro XRD analysis.

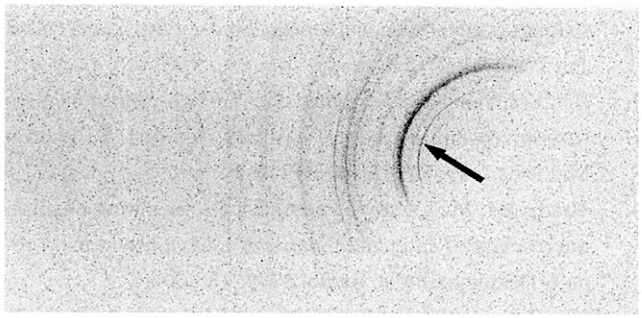

Fig. 3. Micro-XRD IP image from a 100 μm in diameter point on the section of the sialolith. The right portion of the image was hidden by sample holder. The 002 reflection (arrow) showed arcs in stead of the complete diffraction ring, indicating preferred crystal orientation.

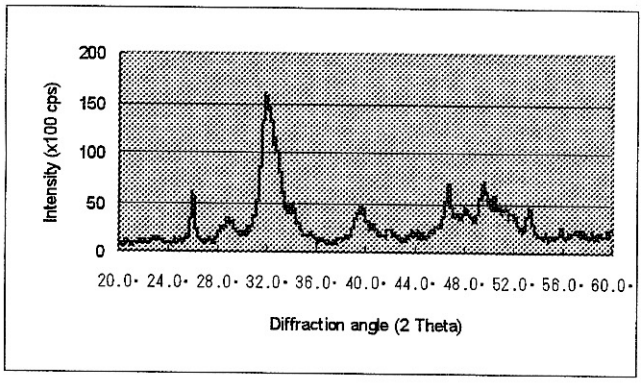

Fig. 5. SA-XRD pattern of the sialolith showing apatite diffraction peaks.

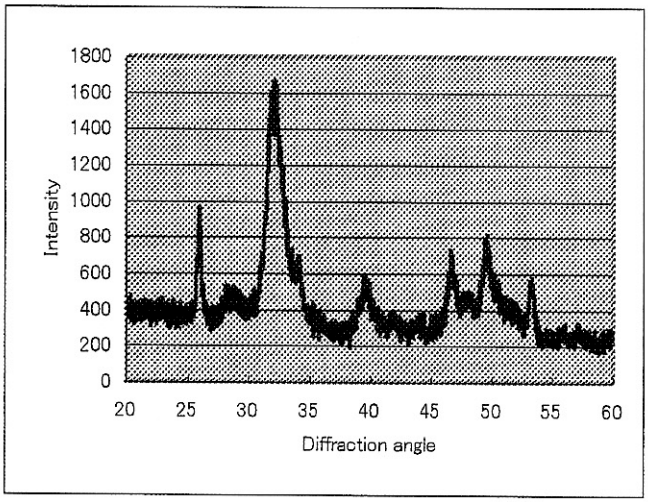

Fig. 2. Conventional XRD pattern of the head-portion section, showing an apatitic diffraction pattern.

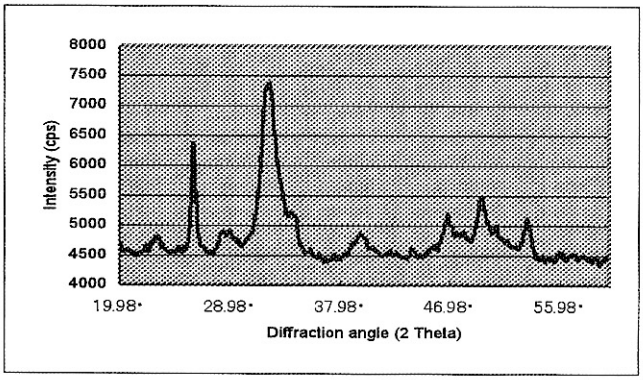

Fig. 4. Converted XRD pattern of the micro-XRD image (Fig. 3) showing the apatite diffraction peaks.

lattice.

The micro FT-IR analysis revealed the main constituent of the sialolith was carbonate apatite, carbonate absorption bands appearing at about 1400 cm^{-1} and 1600 cm^{-1} (Fig. 6).

Discussion

In this study, three types of XRD were applied to reveal the crystallographic characters of the sialolith. The conventional XRD

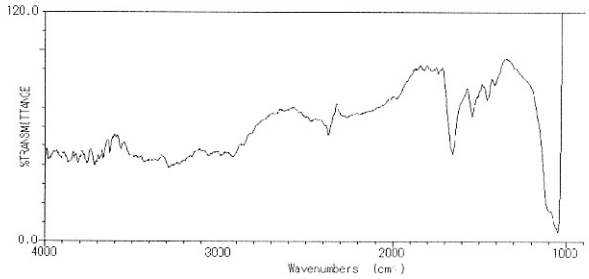

Fig. 6. Micro FT-IR spectrum of the sialolith showing the absorption bands of phosphate ions at about 1050 cm^{-1} and the bands of carbonate ions at about 1450 cm^{-1} and 1550 cm^{-1}.

Table 1. Crystallographic values (unit cell dimenstions) of apatite crystals from different areas of the sialolith analyzed using selected-area XRD.

position No.	a-axis length* (Angstrom)	b-axis length* (Angstrom)
Head 01-1	9.412(11)	6.893(12)
Head 02-1	9.433(16)	6.888(18)
Head 03-1	9.426(25)	6.889(21)
Tail 01-1	9.405(23)	6.903(26)
Tail 01-2	9.430(15)	6.900(12)
Tail 01-3	9.440(22)	6.871(19)
Tail 02-1	9.421(14)	6.886(11)
Tail 03-1	9.431(18)	6.880(13)
Tail 04-1	9.423(10)	6.874(08)

*: The estimated standard deviations were represented in parenthesis.

showed the sialolith being composed of apatite. The micro-XRD showed the preferred crystal orientation in the sialolith. SA-XRD analysis, used for the first time in the analysis of pathological calcifications revealed inhomogeneity in the chemical composition of apatite from layer to layer. The intermittent growth of the apatite crystals was confirmed by crystal orientation analysis.

X-ray diffraction analysis provided information on the crystalline phases present in the sialolith[7, 8]. However, in the present study, the diffraction peaks of the apatite crystals in the sialolith were too broad to allow accurate analysis. Variations in the unit cell dimensions strongly suggested changes in apatite composition, reflecting changes in the environmental condition and composition[7].

Information on the crystalline phase, composition and orientation, could lead to a better understanding of the formation mechanism of sialolith and may provide insights on the appropriate treatment regimen for lithotrypsy[9, 10].

Acknowledgements

The authors thank Professor Isamu Sato, Director of LEBRA (Laboratory for Electron Beam Research and Application), Institute of Quantum Science of the Nihon University, for the opportunity to use the RIGAKU RINT-RAPID and RIGAKU RINT- 2000 X-ray diffraction instruments This study was supported in part by the Frontier Science Project granted from the MECSST, Japan.

References

1. Akimoto Y, Kaneda T, Fujii A, et al. A long submandibular sialolith lying in the Wharton's duct. In: Fuchihata H, ed., Oral and Maxillofacial Radiology Today, Elsevier, 2000; 615-7.
2. Yamamoto H, Sakae T, Takagi M, Otake S. Scanning electron microscopic and X-ray microdiffractometeric studies on sialolith-crystals in human submandibular glands. Acta Pathol Jpn 1984; 34: 47-53.
3. Tohda H, Yamakura K, Yanagisawa T. High-resolution electron microscopic study of salivary calculus. J Electron Microsc (Tokyo) 1995; 44: 399-404.
4. Brady JM, McKinney L, Stanback JS. Scanning electron microscopy of submandibular sialoliths: a preliminary report. Dentomaxillofac Radiol 1989; 18: 42-4.
5. Sakae T, Yamamoto H, Hirai G. Mode of occurrence of brushite and whitlockite in a sialolith. J Dent Res 1981; 60: 842-4.
6. Boskey AL, Burstein LS, Mandel ID. Phospholipids associated with human parotid gland sialoliths. Arch Oral Biol 1983; 28: 655-7.
7. LeGeros RZ. Calcium Phosphates in Oral Biology and Medicine. Basel: Karger, 1991: 130-153.
8. McCONNEL D. Apatite. New York: Springer-Verlag, 1973:111.
9. Iro H, Nitsche N, Meier J et al. Piezoelectric shock wave lithotripsy of salivary gland stones: an in vitro feasibility study. J Lithotr Stone Dis 1991; 3: 211-6.
10. Korago AA, Matina VN, Veroman VIu et al. The composition and structure of salivary calculi (sialoliths) Stomatologiia (Mosk) 1993; 72: 7-12.

Key Engineering Materials Vols. 240-242 (2003) pp. 395-398

Bone Formation Induced by Several Carbonate- and Fluoride-Containing Apatite Implanted in Dog Mandible

T. Sakae,[1] A. Ookubo,[2] R.Z LeGeros[3]
R. Shimogoryou,[2] Y. Sato,[1]
S. Lin[3], H. Yamamoto,[1] Y. Kozawa[1]
[1] Nihon University, School of Dentistry at Matsudo, Chiba, 271-8587, Japan.
[2] Japan Institute for Advanced Dentistry, Nagasaki, Japan.
[3] New York University, College of Dentistry, NY, USA.
sakae@mascat.nihon-u.ac.jp

Keywords: Carbonate, Fluoride, Apatite, Implant, Dog Mandible, Bone graft, Histology, Animal Studies

Abstract Synthetic hydroxyapatite (HAP), carbonate-apatite (CHA) and carbonate-fluoride-apatite (CFA) were implanted into dog mandible bone for 2, 3, 4, 5 and 6 weeks. The chemical composition and crystallographic properties of the synthetic apatites were examined using FT-IR, TG-DTA, AAS and X-ray diffraction. The comparative resorption in vivo for the experimental period was in the order: CHA >> CFA > HAP. CHA formed new bone comparable with the sham-control, and CFA induced fast bone-remodeling and newly formed Haversian system. The results confirmed that CHA are potential bone-grafting materials and also showed that CFA, compared to CHA or HAP materials, accelerate bone formation.

Introduction

Carbonate- and/or fluoride-containing calcium hydroxyapatite are considered as possible bone graft materials [1-3]. *In vitro* and *in* vivo studies showed that fluoride present in synthetic or bone apatite enhances osteoblastic activity [3, 4]. *In vitro* studies also showed that fluoride-containing apatite inhbited osteoclastic activity [5].The aim of this study was to compare the biocompatibility and bio-degradation carbonate- and fluoride-containing apatites implanted in dog mandible bone.

Materials and Methods

Carbonate hydroxyapatite (CHA), carbonate- and fluoride-containing apatite (CFA) and carbonate- and fluoride-free apatite (HAP) were synthesized according to methods previously described [6, 7]. Their chemical and crystallographic properties were determined using X-ray diffraction (XRD), FT-IR, thermogravimetry (TG-DTA), and AAS. The materials were powdered, sieved with 200-mesh, sterilized and implanted in surgically created holes (3mm diameter) in the mandible of Beagle dogs. The implanted materials were covered with biodegradable membranes to prevent material loss during the experiment. After 2, 3, 4, 5, and 6 weeks, the dogs were sacrificed under anesthesia. Histological stained sections of the mandible bones were observed using a microscope.

Results

XRD analysis confirmed the substitution of carbonate (CO_3) and fluoride (F) in the apatite structure based on shifts in diffraction peaks reflecting lattice parameter changes due to CO_3-for-PO_4 and F-for-OH substitutions in calcium hydroxyapatite, $Ca_{10}(PO_4)_6(OH)_2$. Carbonate substitution in CHA and in CFA was demonstrated as the absorbance bands at about 1400 to 1560 and at about 770 to 800 cm-1 in the FT-IR spectra[7] and the weight losses above 400°C in TG-DTA.
Histological sections of these materials showed a clear difference in the extent of resorption or dissolution of the implanted apatites and in the pattern and type of bone formation. HAP remained even after 6 weeks, CHA disappeared after 2 weeks, and CFA disappeared after about 4 weeks (Table 1). After 6 weeks, although the bone formation or induction started earlier, all the implants

formed bone. The new bone formed associated with the materials gave the following characteristics: HAP-induced bone showed characteristics of immature bone in the very early stage; CHA-induced bone was in a more advanced stage but remodeling had not occurred; and CFA-induced bone was the most advanced and showed Haversian system indicating that bone remodeling had started.

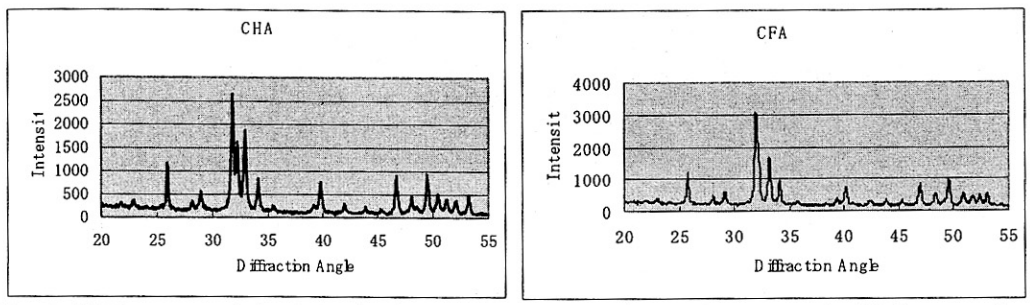

Fig. 1. XRD pattern of the CHA (Left) and the CFA (Right), showing the peak-shift between them indicating the ionic-substitution.

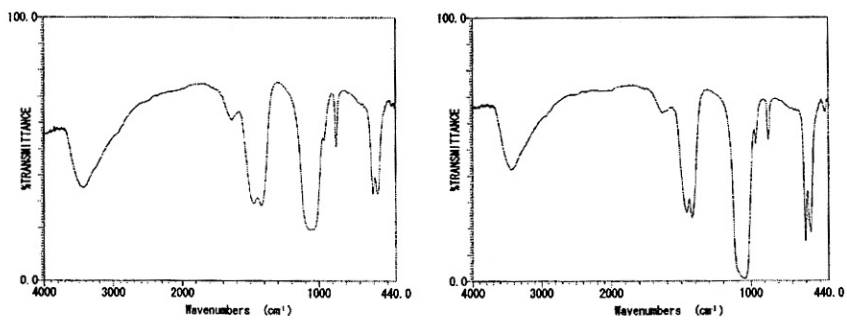

Fig. 2. FT-IR pattern of the CHA (Left), and the CFA (Right), indicating that the CHA containing the more carbonate content than the CFA.

Table 1. Comparison of bone formation pattern for HAP, CHA, CFA implanted in dog mandible.

Type	After 2 weeks	After 6 weeks
HAP	remain	remain
CHA	dissolved	Immature bone
CFA	remain	Haversian

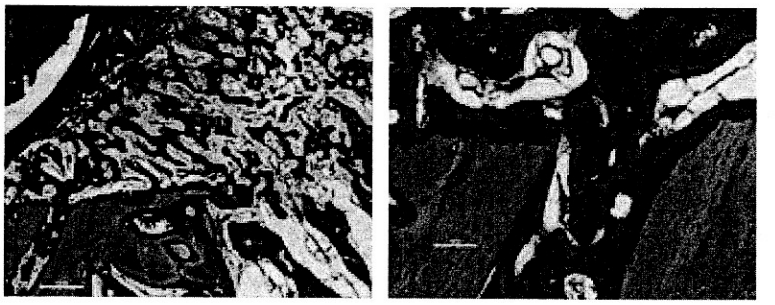

Fig. 3. Bone formation after 2w in the control (Left, x2), and high power view (Right, x10).

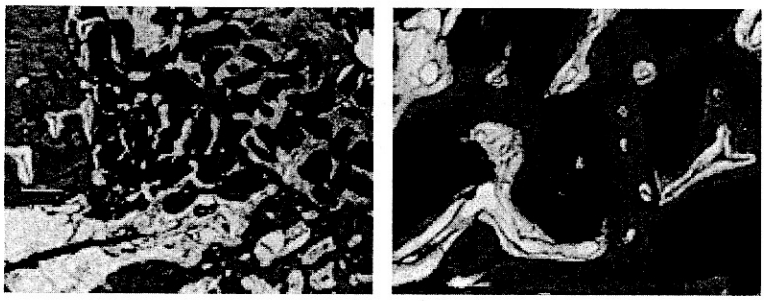

Fig. 4. HAP implanted after 2w (Left, x2), and high power view (Right, x10).

Fig.5. CHA implanted after 4w (Left, x2) and high power view (Right, x10)

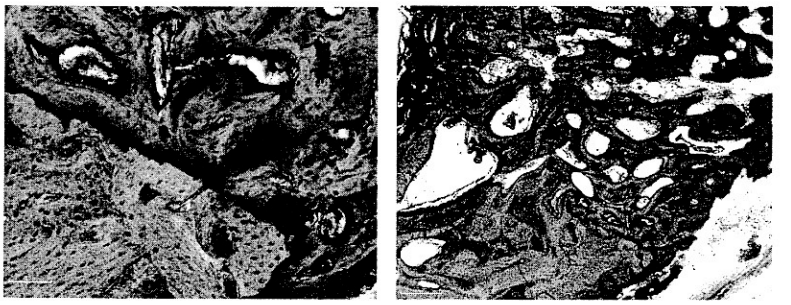

Fig. 6. CFA implanted after 4w (Left, x2), and high power view (Right, x10).

Discussion and Conclusions

This study demonstrated that unsubtituted apatite (HAP), carbonate-substituted (CHA) and carbonate and fluoride-substituted apatite (CFA) materials all formed bone after six weeks when implanted in dog mandible bone. However, these materials differed in extent of resorption with CHA being the fastest and HAP the slowest. These materials also differed in the pattern and type of new bone formed: CFA demonstrated accelerated Haversian bone formation; CHA was associated with immature bone but a later stage of development than HAP.
These results confirmed that carbonate-containing apatites are potential bone-grafting materials. The results also showed that CFA, compared to CHA or HAP materials, accelerate bone formation attributed to the F content. Further studies need to be done to determine the critical amount of F required for maximum effect on bone formation without causing disease (e.g., fluorosis).

Acknowledgements

This study was supported by research grants from the Frontier Science Project from the MECSST, Japan (T.S.), the National Institute for Dental and Cranio-facial Research of NIH (RZL) and the L. Linkow Professorship in Implant Dentistry (RZL). The authors thank to Prof. I. Sato at LEBRA (Laboratory for Electron Beam Research and Application), Institute of Quantum Science, Nihon University for the use of his facilities.

References

[1] C. Frondoza, *et al.*: Bioceramics 11 (1998), p.289.
[2] A. M. Gatti, *et al.*: Bioceramics 11 (1998), p.399.
[3] M. Okazaki, *et al.*: Bioceramics 12 (1999), p.337.
[4] J. Kazimiroff, *et al.*: Bioceramics 9 (1997), p.169.
[5] T. Sakae, *et al.*: Key Engineering Materilas 192-195 (2001), p.347.
[6] R. Z. LeGeros, and M. Tung: Caries Res 17 (1983), p.419.
[7] R.Z. LeGeros, and S. Suga: Calcif Tissue Int 32 (1980), p.169.